Introduction to the electronic structure, luminescence, and magnetism of lanthanides

1

Liviu Ungur[*,†]
*KU Leuven, Leuven, Belgium, †National University of Singapore, Singapore

1.1 Introduction

Lanthanide ions are at the core of many important applications given their unique electronic, optical [1–9], magnetic [10–16], and catalytic [17–20] properties. The large intrinsic magnetic moment of lanthanide ions defines the blocking of magnetization behavior in molecular nanomagnets [21–23] and also plays an important role in strong macroscopic permanent magnet materials, such as $Nd_2Fe_{14}B$ [24–26]. The sharp and intense luminescence displayed by lanthanide ions in various crystal environments is due to the narrow-band transitions between states with different electric/magnetic dipole moments. Lanthanides are also employed as contrast agents in magnetic resonance imaging medical investigations [2,27,28] and serve as important ingredients in commercial lasers [29]. The list of industrial and scientific applications of lanthanide ions is far from being complete. Some of the applications of lanthanides are shown in the following chapters of the present book. The purpose of this chapter is to describe the basic features of the electronic structure of lanthanide ions and to review theories used to explain their electronic structure, optical and magnetic properties.

1.1.1 Free lanthanide ions: Electronic spectra and nature of wave functions

In the absence of ligand environment, the electronic structure of free atoms is defined by the electrostatic interactions between each of the electrons and the central nucleus. In the simplest Hartree-Fock approximation, each electron feels the potential of the nucleus combined with an averaged potential of all the other electrons in the system. In this approximation, the wave function of each electron depends on four quantum numbers (n, l, m, and m_s) and may be expressed as follows:

$$\psi_{nlmm_s}(\boldsymbol{r},\sigma) = R_{nl}(r)Y_l^m(\theta,\varphi)\chi_{m_s}(\sigma) \tag{1.1}$$

where $R_{nl}(r)$ is the one-electron radial wave function, which depends only on the distance to the nucleus (r); $Y_l^m(\theta,\varphi)$ is spherical harmonics; and $\chi_{m_s}(\sigma)$ is spin eigenstates of the electron ($m_s = \pm 1/2$). $\mathbf{r}(r,\theta,\varphi)$ is the position vector of the electron.

Lanthanide-Based Multifunctional Materials. https://doi.org/10.1016/B978-0-12-813840-3.00001-6

These one-electron eigenstates (Eq. 1.1) are used as basis states in the representation of the multielectronic atoms.

Electrons in free lanthanide ions are coupled and form *configurations* (nl^N), in the first approximation. An electronic configuration is a definite arrangement of all electrons in atomic-like orbitals. Ground electronic configuration of neutral free lanthanide atoms is [Xe]$5d^0 6s^2 4f^{N+1}$, with small exceptions for La, Ce, Gd, and Lu, for which the ground configuration is [Xe]$5d^1 6s^2 4f^N$. In common complexes, the outer shell electrons spanning the atomic $5d$ and $6s$ orbitals possess relatively large radii and are highly susceptible to ligand field, and generally, the three outer electrons can be easily removed from the free lanthanide ion system. The relatively low ionization potential is due to the screening effects, which notably weaken the Coulomb interaction between $5d$ and $6s$ electrons and the nucleus [30,31]. The remaining triply ionized configuration for Ln^{3+} ([Xe]$4f^N 5d^0 6s^0$) is very stable for the entire lanthanide series and dominates the wave function in the ground state. Relatively stable chemical compounds with Ce^{4+}, Sm^{2+}, Eu^{2+}, Tb^{4+}, Tb^{2+}, Dy^{2+}, and Yb^{2+} are also known [32–34]. In the present introductory chapter, we will restrict the discussion to the most common oxidation state (3+) of lanthanide ions.

Since the electronic configuration of the [Xe] core is similar for the entire series of lanthanides, one may conclude that it is the *partial filling* of the $4f^N$ shell ($1 \leq n < 14$) that defines the properties of lanthanide ions. For the triply ionized lanthanide ions, excited electronic configurations like [Xe]$4f^{N-1}5d^1$, [Xe]$4f^{N-1}6s^1$, or [Xe]$4f^{N-1}6p^1$ are usually much higher in energy compared with the ground configuration ($>5\times10^4$ cm^{-1}) [35] and are used in various spectroscopic techniques.

The N-electronic wave function of any configuration must respect the Pauli antisymmetry principle, which states that the wave function must change its sign when any two electrons exchange their coordinates. The most straightforward way to account for this principle is to represent the multielectronic wave function in the form of a Slater determinant:

$$\Psi_{\alpha_1,\alpha_2,\ldots,\alpha_N}(\boldsymbol{r_1},\sigma_1,\boldsymbol{r_2},\sigma_2,\ldots\boldsymbol{r_N},\sigma_N) = \frac{1}{\sqrt{N!}}\begin{vmatrix} \psi_{\alpha_1}(\boldsymbol{r_1},\sigma_1) & \psi_{\alpha_1}(\boldsymbol{r_2},\sigma_2) & \ldots & \psi_{\alpha_1}(\boldsymbol{r_N},\sigma_N) \\ \psi_{\alpha_2}(\boldsymbol{r_1},\sigma_1) & \psi_{\alpha_2}(\boldsymbol{r_2},\sigma_2) & \ldots & \psi_{\alpha_2}(\boldsymbol{r_N},\sigma_N) \\ \vdots & \vdots & \ddots & \vdots \\ \psi_{\alpha_N}(\boldsymbol{r_1},\sigma_1) & \psi_{\alpha_N}(\boldsymbol{r_2},\sigma_2) & \ldots & \psi_{\alpha_N}(\boldsymbol{r_N},\sigma_N) \end{vmatrix} \tag{1.2}$$

where α_i represents all quantum numbers (n, l, m, and m_s) of electron i, while $\psi_{\alpha_i}(\boldsymbol{r_i},\sigma_i)$ is monoelectronic wave functions, in the form given by Eq. (1.1).

In general, the energy state corresponding to a given configuration (e.g., $4f^N$ or $4f^{N-1}5d^1$) is highly degenerate. This means that there are many different Slater determinants corresponding to the same energy. Indeed, even though the main quantum numbers for the $4f^N$ configuration are well defined ($n=4$ and $l=3$), the projection of the orbital momenta m of each electron can take any value from -3 to +3, while spin projection m_s may have either one of the two values α ($m_s=+1/2$) or β ($m_s=-1/2$). As a simple example, we may take Ce^{3+}, which has the ground

configuration [Xe]$4f^1$. The unpaired electron of the last shell may occupy any of the seven *f* orbitals, while the spin projection may be either α or β. For this electronic configuration, there are $7\times2=14$ Slater determinants that are equally probable (in the absence of other interactions).

1.1.2 Coulomb repulsion effects

The degeneracy of the $4f^N$ configurations where $N>1$ is partly removed by electron correlation and intraionic spin-orbit coupling effects. The most important correlation effects include the Coulomb interaction (repulsion) between the N unpaired electrons from the last shell and exchange interaction between them. Within the one-electron picture approach, the effect of the core electrons ([Xe]) on the $4f^N$ shell is constant, does not lead to splitting and therefore will not be considered in the discussion. The orbital states that arise after full-electron correlation within a given configuration is considered are called *terms*. In the case of free ions, terms are also highly degenerate. From another perspective, terms of a given N-electron system in spherical symmetry are characterized by a given total spin (S) and total orbital momenta (L), following the principle of conservation of angular momenta for an N-particle system. This results also from the general considerations of commutativity of the electronic Hamiltonian and the operators of total orbital and spin momenta, $\mathbf{L}^2$ and $\mathbf{S}^2$. Since terms correspond to different irreducible representations of the spherical symmetry group, they are not bound to have the same energy. It is convenient to recall Hund's rules for the term's energy:

- Among all possible terms of a given configuration, the terms with the largest total *spin* multiplicity ($2S+1$) have the lowest energy.
- Among all possible terms with the largest total spin multiplicity ($2S+1$), the term with the largest total *orbital* momentum has the lowest energy.

There are many possibilities to combine individual electron's spin and angular momenta in a many-particle system to build eigenstates of a given term, for instance, by following addition rules for angular momenta [36]. Total degeneracy (number of states with the same energy) of a term with definite values of L and S is $(2L+1)(2S+1)$.

Energy spread of different terms arising from the same configuration is of the order of $\sim10^5$ cm^{-1}, while the energy difference between the ground and first excited terms is in the order of $\sim10^4$ cm^{-1}. Terms are denoted by ^{2S+1}L, where S is the total spin and L is the letter defining the total orbital momentum ($L=0$, 1, 2, 3, 4, 5, 6, 7, 8, 9, … → S, P, D, F, G, H, I, K, L, M, …). As an example, the ground term of Ce^{3+} ion ($4f^1$, $L=3$, $S=1/2$) discussed above is ^2F. In certain cases, terms with the same quantum numbers L and S may arise from different electron configurations. Such terms interact with each other via the electronic Hamiltonian.

Sometimes, it is convenient to represent the eigenstates of a given term as $|L,S,M_L,M_S\rangle$, where M_L and M_S are projections of the total orbital and total spin momenta, rather than in a linear expansion of Slater determinants.

1.1.3 Spin-orbit coupling

Spin-orbit coupling is an intrinsic effect of relativistic origin that leads to partial removal of degeneracy of electronic terms. It may be regarded as the interaction of the spin (s) of the electron with the magnetic field created by the same electron while moving in the closed orbit (l):

$$\begin{aligned} \widehat{H}_{so} &= \pm\xi(r)\ \vec{l}\cdot\vec{s} \\ \xi(r) &= -\frac{e}{2m^2c^2}\frac{1}{r}\frac{\partial V(r)}{\partial r} \end{aligned} \tag{1.3}$$

where $V(r)$ is the potential of the central nucleus, c is the speed of light, m is the mass of the electron, r is the distance to the nucleus, and e is the electron charge. Within the first-order perturbation theory, the effect of spin-orbit interaction is dominated by the constant:

$$\zeta_{nl} = \hbar^2 \int \xi(r) R_{nl}^2(r) r^2 dr \tag{1.4}$$

For a nucleus with potential $V = Ze/r$, the spin-orbit coupling depends on the given electron configuration nl:

$$\zeta_{nl} \sim \frac{Z^4}{n^3 l(l+1)\left(l+\frac{1}{2}\right)} \tag{1.5}$$

From Eq. (1.5), it is clear that the spin-orbit coupling constant is strongly dependent on the atomic number Z, so it is element specific. For lanthanide ions, the effect of spin-orbit coupling is still reasonably described in the Russell-Saunders coupling scheme, that is, the effect of spin-orbit coupling on the radial functions is minor, and Eq. (1.1) is valid. For heavy atoms, the representation of the wave function as a product between orbital and spin functions (as in Eq. 1.1) is not accurate. In those cases, electron correlation effects and spin-orbit coupling must be simultaneously accounted, in the relativistic framework, by solving the two- or the four-component Dirac equation [37,38].

Spin-orbit interaction in a given term with definite total orbital L and spin S momenta is approximately given by

$$\widehat{H}_{so} = \pm\frac{\zeta_{nl}}{2S}\widehat{L}\cdot\hat{S} \tag{1.6}$$

where ζ_{nl} is the one-electron spin-orbit coupling constant for the ground configuration nl of the metal ion [39]. The negative sign in Eq. (1.6) is for elements with more-than-half-filled shell, i.e., from Tb^{3+} to Yb^{3+}. Approximate values of the ζ_{4f} parameter for the entire lanthanide series as extracted from NIST data are given in Table 1.1.

Table 1.1 Basic information regarding the ground state of free lanthanide ions

Ion	Ground config.	Total multiplicity	Number of terms	Number of multiplets	Ground term	Ground multiplet	First excited multiplet	Energy difference (cm^{-1})	One-electron spin-orbit coupling parameter, ζ_{4f} (cm^{-1})[a]
Ce^{3+}	$4f^1$	14	1	2	^2F	$^2F_{5/2}$	$^2F_{7/2}$	2253	643
Pr^{3+}	$4f^2$	91	7	13	^3H	$^3H_4$	$^3H_5$	2152	798
Nd^{3+}	$4f^3$	364	17	41	^4I	$^4I_{9/2}$	$^4I_{11/2}$	1880	909
Pm^{3+}	$4f^4$	1001	47	107	^5I	$^5I_4$	$^5I_5$	1490	1012
Sm^{3+}	$4f^5$	2002	73	198	^6H	$^6H_{5/2}$	$^6H_{7/2}$	1080	1175
Eu^{3+}	$4f^6$	3003	119	295	^7F	$^7F_0$	$^7F_1$	370	1410
Gd^{3+}	$4f^7$	3432	119	327	^8S	$^8S_{7/2}$	$^6P_{7/2}$[b]	32,120[b]	–
Tb^{3+}	$4f^8$	3003	119	295	^7F	$^7F_6$	$^7F_5$	2052	1614
Dy^{3+}	$4f^9$	2002	73	198	^6H	$^6H_{15/2}$	$^6H_{13/2}$	3460	1835
Ho^{3+}	$4f^{10}$	1001	47	107	^5I	$^5I_8$	$^5I_7$	5050	2024
Er^{3+}	$4f^{11}$	364	17	41	^4I	$^4I_{15/2}$	$^4I_{13/2}$	6480	1899
Tm^{3+}	$4f^{12}$	91	7	13	^3H	$^3H_6$	$^3H_5$	8090	2244
Yb^{3+}	$4f^{13}$	14	1	2	^2F	$^2F_{7/2}$	$^2F_{5/2}$	10,214	2918

Energy differences correspond to NIST data [35]. The spin-orbit coupling parameter is extracted from the NIST data and Eq. (1.6).
[a] ζ_{4f} was extracted by using the NIST data for the J multiplets originating from the ground LS term to best fit (Eq. 1.6).
[b] Spin-orbit coupling is absent for the ground state of Gd^{3+}: $L = 0$ and $J = S$.

Since the spin-orbit operator in Eq. (1.6) does not commute with the $\mathbf{L}^2$ and $\mathbf{S}^2$ operators, these quantum numbers are not conserved. Instead, the spin-orbit Hamiltonian in Eq. (1.6) commutes with the square of the total angular momentum $\mathbf{J}^2$, implying that only the total angular momenta quantum number $J = L+S$ is conserved. Following the rules for addition of two angular momenta, the quantum number J takes positive values running from $|L-S|$ to $L+S$, with a step of 1. As an example, spin-orbit interaction within the ground ^3F term of Pr^{3+} ion ($L=3$, $S=1$) splits it in three *multiplets* with $J_1=(3-1)=2$, $J_2=(3-1+1)=3$, and $J_3=(3-1+2)=(3+1)=4$. In order to uniquely identify the multiplets originating from various terms, they are written in the format: $^{2S+1}L_J$. For example, the three multiplets arising from the ^3F term are $^3F_2$, $^3F_3$, and $^3F_4$. Hund's rule coupling allows to determine which of the multiplets will be in the ground state:

- Among all possible multiplets arising from the ground term, the lowest will be $J=|L-S|$ for a less-than-half-filled *nl* shell and $J=L+S$ for a more-than-half-filled *nl* shell.

In order to compute the energies corresponding to the J eigenstates, we need to rewrite the spin-orbit Hamiltonian as follows:

$$\begin{aligned} J^2 &= (L+S)^2 = L^2+S^2+2LS \\ \widehat{H}_{so} &= \pm\frac{\zeta_{4f}}{2S}\widehat{L}\widehat{S} = \pm\frac{\zeta_{4f}}{4S}\left(\hat{J}^2-\hat{L}^2-\hat{S}^2\right) \end{aligned} \tag{1.7}$$

The $\widehat{H}_{so}$ for a given multiplet is diagonal when written in the basis of $|L,S,J,M_J\rangle$ coupled eigenstates (Eq. 1.5)

$$|L,S,J,M_J\rangle = \sum C^{J,M_J}_{L,M_L,S,M_S}|L,S,M_L,M_S\rangle \tag{1.8}$$

where C^{J,M_J}_{L,M_L,S,M_S} are Clebsch-Gordan coefficients describing the coupling between two angular momenta L and S in a total angular momenta $|J,M_J\rangle$ [36]. Clebsch-Gordan coefficients become *zero* whenever any of the following relations $M_L+M_S \neq M_J$, $M_L \geq L$, $M_S \geq S$, or $M_J \geq J$ are true.

Energies corresponding to individual J states are as follows:

$$E(J) = \frac{\zeta_{4f}}{4S}(J(J+1)-L(L+1)-S(S+1)) \tag{1.9}$$

The energy gap between J and $J-1$ eigenstates is given by the Landé interval rule [40]:

$$E(J)-E(J-1) = \frac{\zeta_{4f}}{4S}(J(J+1)-(J-1)J) = \frac{\zeta_{4f}}{2S}J \tag{1.10}$$

Deviations from the Landé interval rule are noticed for systems containing several unpaired electrons (see Table 1.1 and Fig. 1.1). This is explained by the coupling between identical J multiplets that arise from different LS terms via spin-orbit coupling.

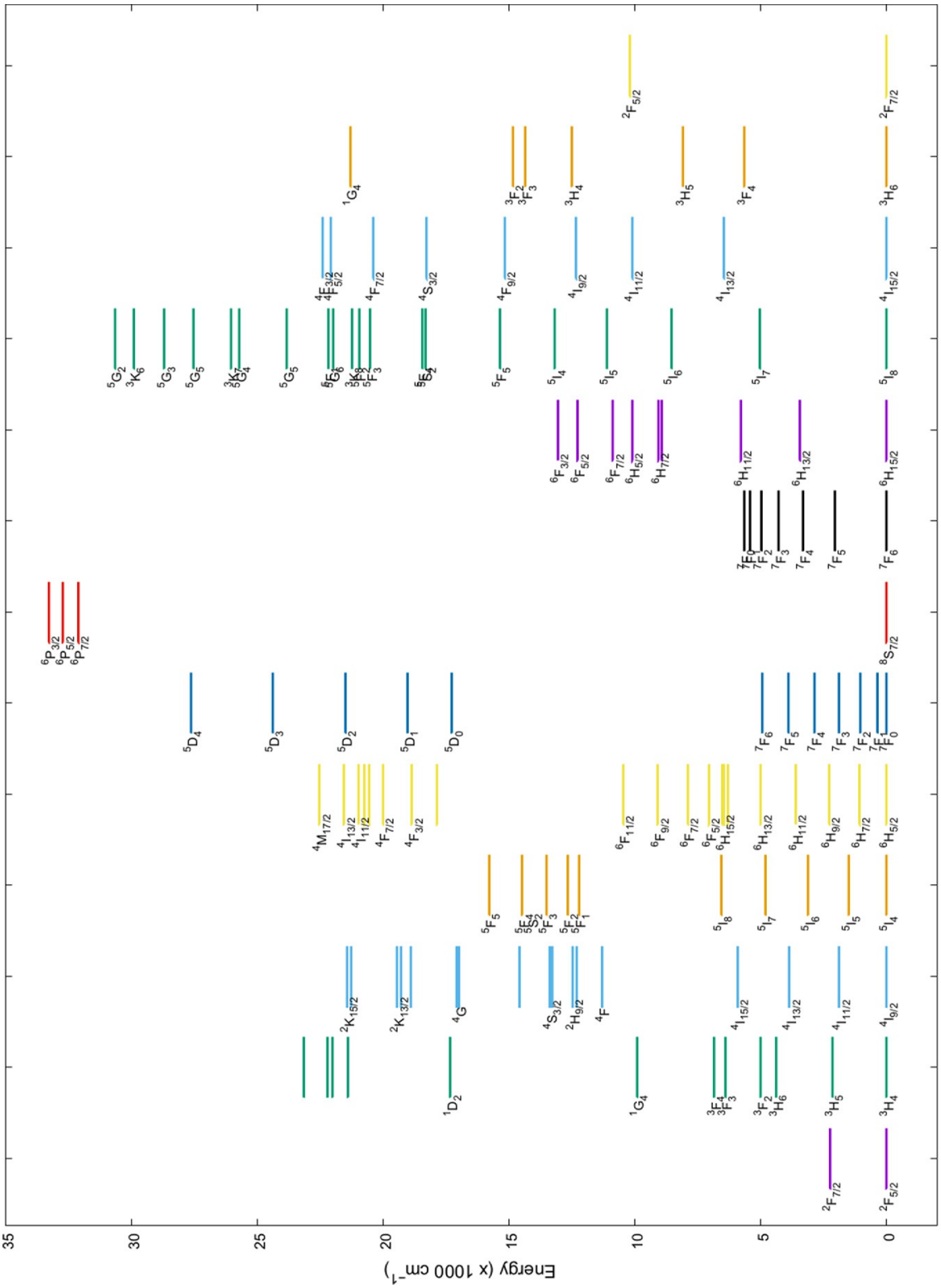

Fig. 1.1 NIST experimental energies [35] of the low-lying multiplets of free Ln^{3+} ions. Labels of some overlapping multiplets are not shown for clarity reasons. Energy states are plotted at the true scale.

1.1.4 Crystal field splitting

When a lanthanide ion is placed in a low-symmetry crystal matrix, each multiplet of the lanthanide becomes further split in individual components, either in Kramers doublets for odd-electron systems (Ce^{3+}, Nd^{3+}, Sm^{3+}, Gd^{3+}, Dy^{3+}, Er^{3+}, and Yb^{3+}) or in individual nondegenerate levels for even-electron systems (Pr^{3+}, Pm^{3+}, Eu^{3+}, Tb^{3+}, Ho^{3+}, and Tm^{3+}). This splitting depends on the properties of the ligand environment and is usually in the order of 300–1500 cm^{-1}. Crystal field theory, which is one of the first to explain the effect of the ligand environment, is based on the following approximations [41,42]:

- Only the 4*f* electrons of the lanthanide are considered. The effect of the metal's core orbitals or virtual (empty) orbitals is neglected.
- The effect of the ligand atoms is limited to providing an external (electrostatic) potential that influences the 4*f* shell. This effect is considered a small perturbation over the free-ion spin-orbit multiplet structure.
- No overlap between metal and ligand's orbitals is considered.

Fig. 1.2 shows a rank of various interactions leading to the splitting of the initial $4f^N$ configuration in lanthanides.

The description of the crystal-field splitting is done via an effective one-electron Hamiltonian:

$$\widehat{H}_{CF} = \sum_{i}^{N} h_{CF}\left(\frac{\boldsymbol{r}_i}{r_i}\right) = \sum_{i}^{N}\sum_{k}\sum_{q=-k}^{k} B_{kq}\widehat{C}_k^q\left(\frac{\boldsymbol{r}_i}{r_i}\right) \tag{1.11}$$

where $h_{CF}\left(\frac{\boldsymbol{r}_i}{r_i}\right)$ is the contribution to the total Hamiltonian from electron i, B_{kq} is the crystal-field parameter of rank k ($k \leq 6$) and projection q, and $\widehat{C}_k^q\left(\frac{\boldsymbol{r}_i}{r_i}\right)$ is the crystal-field operator acting on electron i. It is related to the spherical harmonics multiplied by a coefficient:

$$\widehat{C}_k^q\left(\frac{\boldsymbol{r}_i}{r_i}\right) = \sqrt{\frac{4\pi}{2k+1}}\hat{Y}_k^q\left(\frac{\boldsymbol{r}_i}{r_i}\right) \tag{1.12}$$

The operator in Eq. (1.12) acts on individual electrons of the last shell. It may be proved to be equivalent to a different form of the crystal-field Hamiltonian operator that acts on the ground J multiplet [41,43]:

$$\widehat{H}_{CF} = \sum_{k=2,4,6}\sum_{q=0}^{k}\left(B_k^q\hat{O}_k^q(J) + C_k^q\hat{\Omega}_k^q(J)\right) \tag{1.13}$$

where $\hat{O}_k^q(J)$ and $\hat{\Omega}_k^q(J)$ are the real and the complex combinations of the spherical harmonics (Table 1.2), respectively, with the dimension $2J+1$, B_k^q, and C_k^q corresponding with (real) crystal-field parameters.

It is clear that a direct application of Eq. (1.11) or Eq. (1.13) for a lanthanide in a low-symmetry environment requires knowledge of the entire set of 27 B_k^q parameters. One approach to compute the B_k^q parameters is to use the point-charge model (PCM) [40,44–46]. In this model, the B_{kq} parameters (Eq. 1.11) are given by the effective

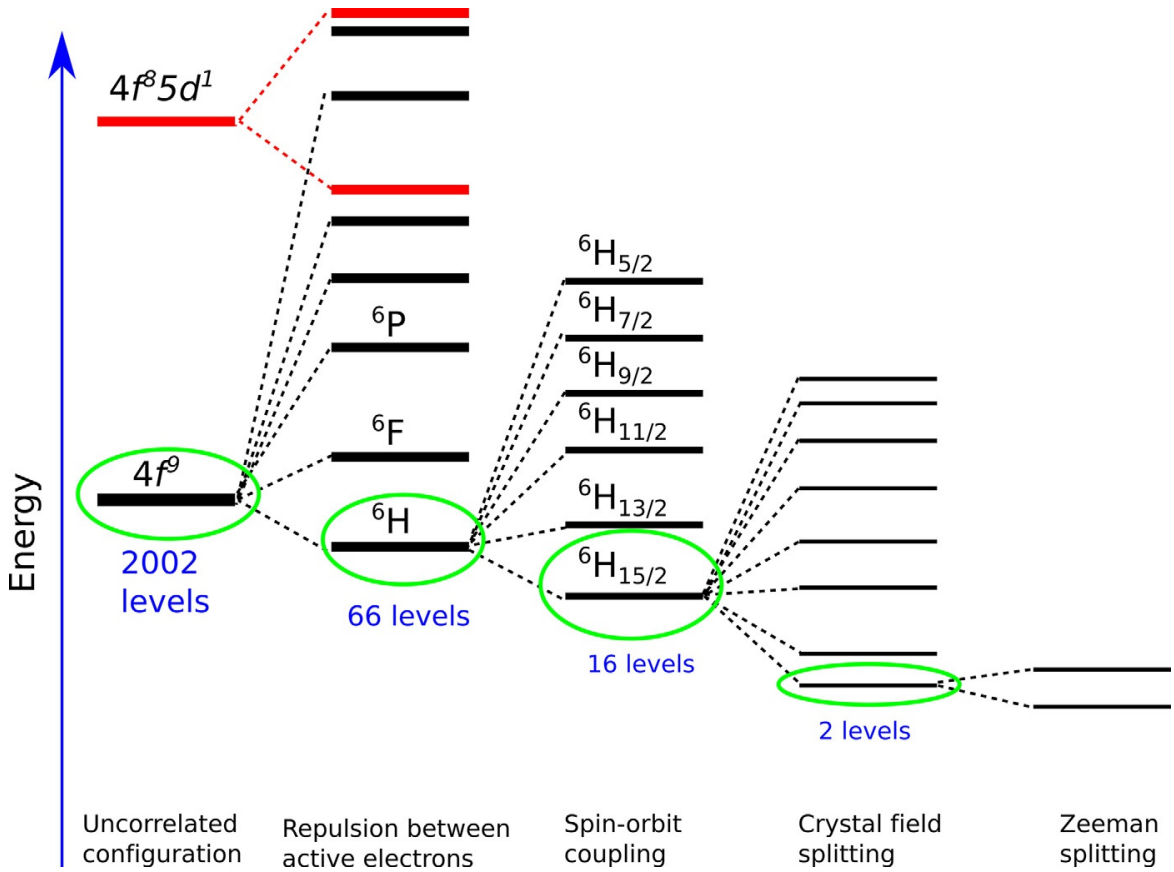

Fig. 1.2 Effect of various interactions on the splitting of the degenerate $4f^9$ configuration of the free Dy^{3+} ion. Interactions are ranked from strong (*left*) to weak (*right*). Only the splitting of the ground state is shown for clarity, while it should be understood that excited states are subject to similar splitting effects. As a result of all interactions, on the right-hand side of the picture, the individual levels are thus fairly mixed. Energy splitting is not plotted at scale. Zeeman splitting is caused only by an applied magnetic field.

charge (Z_i) on the neighboring ligand atoms according to their crystallographic positions (r_i, θ_i, and φ_i) as follows:

$$B_{kq} = -e\sum_i \frac{Z_i \hat{Y}_k^q(\theta_i, \varphi_i)}{r_i^{k+1}} \tag{1.14}$$

Directly applied in this form, the PCM gives large deviations from available experimental data. One reason is that the charges on neighbor ligand atoms are not easily determined. Employment of their (chemical) charge only gives a qualitative description of the data.

The crystal field theory is now mainly used as a phenomenological approach. In this model, the Hamiltonian in Eq. (1.13) is computed in the basis of $|L,S,J,M_J\rangle$ spin-orbit eigenstates of the ground J term using some values of the B_k^q parameters and diagonalized. The resulting $2J+1$ eigenstates are used to compute some properties, for example, magnetic susceptibility, molar magnetization, some experimental (known) energy states, and EPR spectra. B_k^q parameters are varied until the standard

Table 1.2 Explicit crystal-field Hamiltonian as a function of the point-group symmetry of the lanthanide

Symmetry	Crystal-field operator
Cubic O, T_d, O_h T, T_h	$\widehat{H}_{CF} = B_4^0\left(\hat{O}_4^0 + 5\hat{O}_4^4\right) + B_6^0\left(\hat{O}_6^0 - 21\hat{O}_6^6\right)$
Hexagonal D_6, C_{6v}, D_{3h}, D_{6h} C_{6h}, C_{3h}, C_6	$\widehat{H}_{CF} = B_4^0\left(\hat{O}_4^0 + 5\hat{O}_4^4\right) + B_6^0\left(\hat{O}_6^0 - 21\hat{O}_6^6\right) + B_6^2\left(\hat{O}_6^2 - \hat{O}_6^6\right)$ $\widehat{H}_{CF} = B_2^0\hat{O}_2^0 + B_4^0\hat{O}_4^0 + B_6^0\hat{O}_6^0 + B_6^6\hat{O}_6^6$ $\widehat{H}_{CF} = B_2^0\hat{O}_2^0 + B_4^0\hat{O}_4^0 + B_6^0\hat{O}_6^0 + B_6^6\hat{O}_6^6 + C_6^6\hat{\Omega}_6^6$
Trigonal D_3, C_{3v}, D_{3d} C_3, C_{3i}	$\widehat{H}_{CF} = B_2^0\hat{O}_2^0 + B_4^0\hat{O}_4^0 + B_6^0\hat{O}_6^0 + B_4^3\hat{O}_4^3 + B_6^3\hat{O}_6^3 + B_6^6\hat{O}_6^6$ $\widehat{H}_{CF} = B_2^0\hat{O}_2^0 + B_4^0\hat{O}_4^0 + B_6^0\hat{O}_6^0 + B_4^3\hat{O}_4^3 + C_4^3\hat{\Omega}_4^3 + B_6^3\hat{O}_6^3 + C_6^3\hat{\Omega}_6^3 + B_6^6\hat{O}_6^6 + C_6^6\hat{\Omega}_6^6$
Tetragonal D_4, C_{4v}, D_{2d}, D_{4h} C_4, S_4, C_{4h}	$\widehat{H}_{CF} = B_2^0\hat{O}_2^0 + B_4^0\hat{O}_4^0 + B_6^0\hat{O}_6^0 + B_4^4\hat{O}_4^4 + B_6^4\hat{O}_6^4$ $\widehat{H}_{CF} = B_2^0\hat{O}_2^0 + B_4^0\hat{O}_4^0 + B_6^0\hat{O}_6^0 + B_4^4\hat{O}_4^4 + C_4^4\hat{\Omega}_4^4 + B_6^4\hat{O}_6^4 + C_6^4\hat{\Omega}_6^4$
Orthorhombic D_2, C_{2v}, D_{2h}	$\widehat{H}_{CF} = B_2^0\hat{O}_2^0 + B_2^2\hat{O}_2^2 + B_4^0\hat{O}_4^0 + B_4^2\hat{O}_4^2 + + B_4^4\hat{O}_4^4 + B_6^0\hat{O}_6^0 + B_6^2\hat{O}_6^2 + + B_6^4\hat{O}_6^4 + B_6^6\hat{O}_6^6$
Monoclinic C_2, C_s, C_{2h}	$\widehat{H}_{CF} = B_2^0\hat{O}_2^0 + B_2^2\hat{O}_2^2 + C_2^2\hat{\Omega}_2^2 + B_4^0\hat{O}_4^0 + B_4^2\hat{O}_4^2 + C_4^2\hat{\Omega}_2^2 + B_4^4\hat{O}_4^4 + C_4^4\hat{\Omega}_4^4 + B_6^0\hat{O}_6^0 + B_6^2\hat{O}_6^2 + C_6^2\hat{\Omega}_6^2 + B_6^4\hat{O}_6^4 + C_6^4\hat{\Omega}_6^4 + B_6^6\hat{O}_6^6 + C_6^6\hat{\Omega}_6^6$
Triclinic C_1	$\widehat{H}_{CF} = B_2^0\hat{O}_2^0 + B_2^1\hat{O}_2^1 + C_2^1\hat{\Omega}_2^1 + B_2^2\hat{O}_2^2 + C_2^2\hat{\Omega}_2^2 + B_4^0\hat{O}_4^0 + B_4^1\hat{O}_4^1 + C_4^1\hat{\Omega}_4^1 + B_4^2\hat{O}_4^2 + C_4^2\hat{\Omega}_4^2 + B_4^3\hat{O}_4^3 + C_4^3\hat{\Omega}_4^3 + B_4^4\hat{O}_4^4 + C_4^4\hat{\Omega}_4^4 + B_6^0\hat{O}_6^0$ $+ B_6^1\hat{O}_6^1 + C_6^1\hat{\Omega}_6^1 + B_6^2\hat{O}_6^2 + C_6^2\hat{\Omega}_6^2 + B_6^3\hat{O}_6^3 + C_6^3\hat{\Omega}_6^3 + B_6^4\hat{O}_6^4 + C_6^4\hat{\Omega}_6^4 + B_6^5\hat{O}_6^5 + C_6^5\hat{\Omega}_6^5 + B_6^6\hat{O}_6^6 + C_6^6\hat{\Omega}_6^6$

$\hat{O}_k^q = \frac{1}{2}\left(\hat{Y}_k^q + (-1)^q\hat{Y}_k^{-q}\right)$; $\hat{\Omega}_k^q = \frac{1}{2i}\left(\hat{Y}_k^q - (-1)^q\hat{Y}_k^{-q}\right), q > 0$; B_k^q, C_k^q—real.

deviation between computed and measured data decreases below some chosen threshold. An alternative is to build the crystal-field matrix in the basis of the complete set of eigenstates originating from the $4f^N$ configuration. In such case, the crystal field will also mix excited multiplets, allowing a slightly improved description of the thermodynamic properties (e.g., magnetic susceptibility). The latter method is of choice when optical properties are described.

Some of the negative points of this phenomenological approach are (*i*) the overparameterization problem (impossibility to reliably fit a set of 27 independent parameters, since more than one set would provide the same quality of the description) and (*ii*) the common way of overcoming this difficulty by fitting only 3–4 parameters and disregarding the remaining 23–24 parameters. Symmetry considerations allow to effectively reduce the number of independent parameters. As Table 1.2 shows, the number of crystal-field parameters that need to be considered allows a reliable fit only for the highest point groups, cubic or hexagonal. Compounds with lower symmetry are practically intractable.

Phenomenological approaches involving displacement of ligand charges out of the metal-ligand axis have also been proposed [47]. In some cases, these methods gave a better agreement with experiment. It is important to mention here that even if the method of obtaining the parameters of the crystal field is improved or optimized, the number of independent fitting parameters remains the same. Improvements in the point-charge model and related approaches require to explicitly account for more involved physical effects:

- Effect of further distant ligand atoms
- Spatial distribution of the ligand electron density, including metal-ligand exchange interaction
- Nonorthogonality between metal and ligand's orbitals
- Nonorthogonality between metal's core, 4*f*, and ligand's orbitals
- Multiconfiguration approaches accounting for polarization, covalence, and screening effects

Clearly, a more involved model description increases the number of parameters that need to be determined/provided. As an example, the screening effects of the $5s^2 5p^6$ closed shells on the crystal-field splitting of the $4f^N$ shell is accounted for by a modified crystal-field Hamiltonian:

$$\widehat{H}_{CF} = \sum_{i=1}^{N} \sum_{k=2,4,6} \sum_{q=-k}^{k} B_{kq}(1-\sigma_k)\widehat{C}_k^q\left(\frac{\boldsymbol{r}_i}{r_i}\right) \tag{1.15}$$

where σ_k is additional phenomenological parameters w.r.t. Eq. (1.11). The role of σ_k screening factors is mainly to change the ratio between different rank operators. Similarly, charge penetration effects could be accounted for by additional parameters η_k, which depend on the operator rank [41,48]. As an example, corrected crystal-field parameters are as follows:

$$B_{k0}^{corr} = B_{k0}^{PCM}(1+\eta_k) \tag{1.16}$$

Developments of the crystal field theory to include the (missing) covalent effects along the electrostatic contribution [49] and novel methods based on the parameterization of the metal-ligand covalence interaction, like the angular overlap model, have been developed over time [50,51]. These methods are also mainly phenomenological, since the number of parameters grows significantly in the case of nonequivalent ligands.

There are many computer codes and programs that implement crystal field theory for the computation of electronic structure and properties of lanthanide compounds. Among the most popular ones, we could mention SIMPRE [52,53], PHI [54], CONDON [55], etc.

A recent approach to determine the parameters of the crystal field is to use rigorous *ab initio* quantum chemistry methods [22,56–59]. This approach will be briefly introduced in a latter section.

1.2 Theoretical description of optical behavior of lanthanides

1.2.1 Optical transitions

Lanthanide ions in various hosts display an interesting optical behavior manifested in relatively sharp and intense luminescence, making them important ingredients in the technological design of lasers and various optical sensors. This property of lanthanide ions was quite puzzling for many years, given the inability of existing theories at that time to provide a reasonable explanation of its origin.

From the point of view of electronic structure, energy states in materials are quantized (discrete). Transitions between any two states are accompanied by the absorption or emission of electromagnetic radiation with an energy corresponding to the exact energy difference between the two states (Eq. 1.17 and Fig. 1.3):

$$\left|E_{initial} - E_{final}\right| = \hbar\nu \tag{1.17}$$

There are many physical phenomena that may lead to transitions between two states: electric dipole (ED) transition, magnetic dipole (MD) transition, electric quadrupole (EQ) transition, etc. Eq. (1.18) gives the explicit forms of these operators:

$$\begin{aligned}
\hat{\vec{P}} &= -e\sum_i \hat{\vec{r}}_i \\
\hat{\vec{M}} &= -\frac{e\hbar}{2mc}\sum_i \left(\hat{\vec{l}}_i + 2\hat{\vec{s}}_i\right) \\
\hat{\vec{Q}} &= \frac{1}{2}\sum_i \left(\hat{\vec{k}}_i \cdot \hat{\vec{r}}_i\right)\hat{\vec{r}}_i
\end{aligned} \tag{1.18}$$

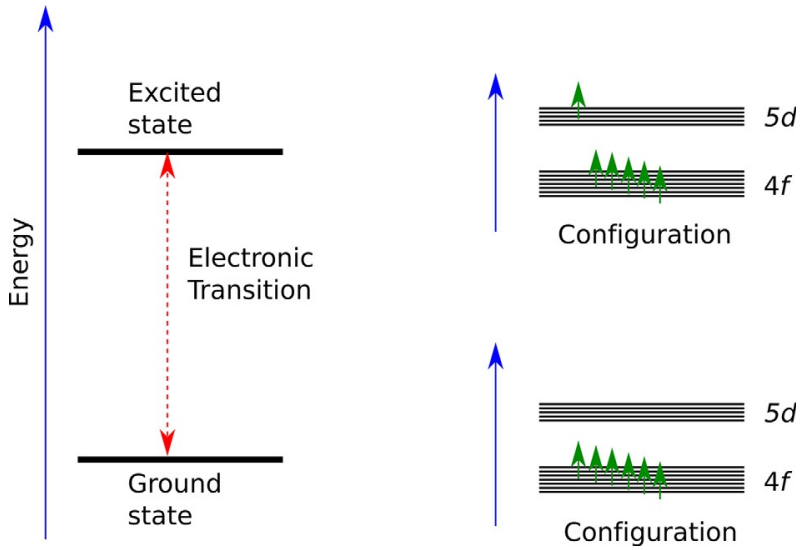

Fig. 1.3 Ground and excited configurations of opposite parity of lanthanide ions. Transition dipole moment between these two states is allowed. Following Judd-Ofelt theory, the opening of the transition dipole moment between the low-lying states (with dominant $4f^N$ character) arises due to the small admixture of the states from excited configurations of opposite parity to the ground states, via crystal-field effect.

The intensity of an electronic transition is proportional to the square of the matrix element of the corresponding operator expressed in the basis of the initial (j) and final (i) wave functions $H_{ij} = \int \psi_i \hat{O} \psi_j d\tau$. The transition is said to be *forbidden* whenever this matrix element is zero, and otherwise, it is *allowed*. Given the fact that all the operators that are responsible for the various transitions (Eq. 1.18) commute with the symmetry operators of the entire system, symmetry rules may be used to determine if a transition is allowed or not. The symmetry characteristics of each component of the operator (e.g., Cartesian axes x, y, or z for electric and magnetic dipole transitions) can be obtained from standard character tables based on the point group to which the molecule or complex belongs. For a qualitative analysis, by following group theoretical rules, only the symmetry of the transition moment function needs to be evaluated: $\psi_i \hat{O} \psi_j$. If this function spans the totally symmetrical representation of the respective group (denoted by A, A_1, A_g, or A', having characters of all group operators as 1), then the transition is allowed, and otherwise, it is forbidden. It is important to mention that, even though some transitions are electronically forbidden, in some cases, the experimental spectra may show those transitions, induced by various effects that were not included in the theoretical approach, for example, vibronic interactions. For a quantitative study of the intensity of transitions, all allowed transition moment matrix elements between all states need to be evaluated.

It is instructive to briefly discuss the electric dipole transitions for lanthanide ions. As previously mentioned, the ground multiplet wave function is a linear combination of Slater determinants with various distributions of N electrons among the $4f$ orbitals, that is, arising from the $4f^N$ ground configuration. For simplicity's sake, let us consider the C_i point group (inversion). All $4f$ orbitals are odd functions with

respect to inversion operation, that is, the $4f$ orbitals change their sign upon inversion operation. This means that, depending on the number of electrons in the $4f$ shell, the total (coupled) wave functions arising from the $4f^N$ configuration will behave according to the same irreducible representation of the inversion point group, being either symmetrical (gerade, g) or antisymmetric (ungerade, u). For example, the wave function of the ground configuration of Tb^{3+}, $N=8$, will have the symmetry: $u\otimes u\otimes u\otimes u\otimes u\otimes u\otimes u\otimes u=g$, that is, gerade (even). Similarly, the wave function of the ground configuration of Dy^{3+} ($N=9$) is found to be ungerade (odd).

The symmetry of the electric dipole operator is ungerade (odd). Applying the inversion operator, we have the following:

$$\hat{C}_i\hat{\vec{P}}=-e\hat{C}_i\sum_i\hat{\vec{r}}_i=-\mathrm{e}\sum_i\hat{C}_i\hat{\vec{r}}_i=-e\sum_i-\hat{\vec{r}}_i=-\hat{\vec{P}} \tag{1.19}$$

The symmetry of the matrix elements of the electric dipole operator over the $4f^N$ wave functions is therefore odd. For $N=$ even, $u\otimes u\otimes u=u$, and for $N=$ odd, $g\otimes u\otimes g=u$. Spatial integral over odd functions is thus zero, which means that electric dipole transitions are not allowed for the wave functions possessing pure $4f^N$ character. Nevertheless, it is an experimental fact that lanthanides show sharp and strong luminescence.

1.2.2 Judd-Ofelt theory

Judd [60] and Ofelt [61] independently proposed a theoretical explanation of the origin of luminescence behavior of lanthanide ions in various crystal hosts and provided practical formulas for the evaluation of the oscillator strengths (intensities) of the observed spectroscopic lines. In this section, we will briefly review the principles and limitations of this theory.

The Judd-Ofelt theory is based on the following assumptions:

- The effect of the crystal environment is considered at the first order of the perturbation theory, that is, it is considered a relatively weak effect w.r.t. free-ion energy structure. Crystal-field effect is described within a pure electrostatic approach (PCM).
- It is assumed that optical transitions are of the electric dipole kind. Given that electric dipole-dipole transitions between $4f^N$ states are forbidden, the ground-state wave function of lanthanide ions in crystals should admix configurations with opposite parity via crystal-field effect, like $4f^{N-1}5d^1$, $4d^94f^{N+1}$, $4f^{N-1}6s^1$, $4f^{N+1}5s^1$, and $4f^{N-1}5g^1$. The matrix elements of the transition electric dipole moment of these configurations with the states of the ground configuration ($4f^N$) are then allowed. The first-order perturbed eigenstates after crystal-field splitting are

$$|\psi_a\rangle=|a\rangle+\sum_k\frac{\langle k|\hat{H}_{CF}|a\rangle}{E_a-E_k}|k\rangle \tag{1.20}$$

where $|k\rangle$ represents the states with opposite parity, while $|a\rangle$ is the initial $4f^N$ eigenstates. In the absence of perturbation (when $\hat{H}_{CF}=0$), the admixture of excited

states becomes zero, recovering the initial $4f^N$ eigenstates. It has to be mentioned here that $\widehat{H}_{CF}$ contains operators of *odd* rank only (1, 3, and 5), to account for the difference in the parity of the $|a\rangle$ and $|k\rangle$ states. The matrix element of the transition electric dipole moment in the basis of two low-lying first-order corrected states $|\psi_a\rangle$ and $|\psi_b\rangle$ becomes

$$\langle \psi_b | \hat{P} | \psi_a \rangle = \sum_k \left[\frac{\langle b | \widehat{H}_{CF} | k \rangle \langle k | \hat{P} | a \rangle}{E_b - E_k} + \frac{\langle b | \hat{P} | k \rangle \langle k | \widehat{H}_{CF} | a \rangle}{E_a - E_k} \right] \tag{1.21}$$

since $\langle a | \hat{P} | b \rangle = \langle b | \hat{P} | a \rangle = 0$ (because $|a\rangle$ and $|b\rangle$ have the same parity; see the discussion above).

Eq. (1.21), even if complete, is not very convenient for practical usage because the number of excited states $|k\rangle$ is quite large. To give an idea of the complexity of the problem, Table 1.3 shows the number of $|a\rangle$ and $|k\rangle$ states in several configurations with opposite parity.

For the direct application of Eq. (1.21), the individual energies of the $|k\rangle$ states must be known. This is not a trivial task, given the fact that the effect of the crystal field might be different on the $|k\rangle$ states compared with its effect on $|a\rangle$ and $|b\rangle$ low-lying states. In order to simplify the problem, the Judd-Ofelt theory comes with several new approximations:

- The effect of the crystal field on the $|k\rangle$ states is neglected: the entire excited configuration $4f^{N-1}5d^1$ is considered degenerate. This is, of course, not completely true, but offers a great simplification.
- The energy difference between $|a\rangle$ and $|b\rangle$ low-lying states is neglected. This makes both denominators in Eq. (1.21) equal (denoted later by $\Delta E_{n'l'}$).

Under these two approximations and considering the full expansion in the $|k\rangle$ states, the two terms appearing in square brackets in Eq. (1.21) can be combined together in one effective tensor operator (of even parity). This is possible because the ED and CF operators considered here are written in a multipole expansion in the form given in Eq. (1.11). In this case, ED operator contains tensors of rank up to one, while CF operator contains only odd components. By applying Wigner-Eckart theorem [36,62–64] after some transformations, the matrix elements of the transition dipole moment may be written as

$$\langle \psi_b | \hat{P} | \psi_a \rangle = \sum_{tp} \sum_{\lambda} (-1)^{p+q} (2\lambda + 1) \begin{pmatrix} 1 & \lambda & t \\ q & -q-p & p \end{pmatrix} A_{tp} \Xi(t, \lambda) \left\langle JM | \hat{U}^{\lambda}_{p+q} | J'M' \right\rangle \tag{1.22}$$

in which t is the (odd) rank of the crystal-field operator (1, 3, or 5), p is its projection (ranging from $-t$ to $+t$), q is the projection of the electric dipole operator $\hat{P}$ (ranging from -1 to $+1$), λ is the total rank of the effective tensor operator ($\lambda = t+1$, even), A_{tp} is the crystal-field parameters (odd rank), and $\left\langle JM | \hat{U}^{\lambda}_{p+q} | J'M' \right\rangle$ is the matrix element

Table 1.3 Multiplicities of some excited configurations with opposite parity considered by the Judd-Ofelt theory

Ion	Ground config.	Total multiplicity	Multiplicity of the $4f^{N-1}5d^1$ configuration	Multiplicity of the $4d^9 4f^{N+1}$ configuration	Multiplicity of the $4f^{N-1}6s^1$ configuration	Multiplicity of the $5s^1 4f^{N+1}$ configuration
Ce^{3+}	$4f^1$	14	10	910	2	182
Pr^{3+}	$4f^2$	91	140	3640	28	728
Nd^{3+}	$4f^3$	364	910	10,010	182	2002
Pm^{3+}	$4f^4$	1001	3640	20,020	728	4004
Sm^{3+}	$4f^5$	2002	10,010	30,030	2002	6006
Eu^{3+}	$4f^6$	3003	20,020	34,320	4004	6864
Gd^{3+}	$4f^7$	3432	30,030	30,030	6006	6006
Tb^{3+}	$4f^8$	3003	34,320	20,020	6864	4004
Dy^{3+}	$4f^9$	2002	30,030	10,010	6006	2002
Ho^{3+}	$4f^{10}$	1001	20,020	3640	4004	728
Er^{3+}	$4f^{11}$	364	10,010	910	2002	182
Tm^{3+}	$4f^{12}$	91	3640	140	728	28
Yb^{3+}	$4f^{13}$	14	910	10	182	2

of the total effective tensor operator between multiplets of the ground-state configuration (of the $4f^N$ kind). It can be further simplified to

$$\left\langle JM\right|\hat{U}^{\lambda}_{p+q}\left|J'M'\right\rangle = (-1)^{J-M}\begin{pmatrix} J & \lambda & J' \\ -M & p+q & M' \end{pmatrix}\left\langle J\left\|\hat{U}^{\lambda}\right\|J'\right\rangle$$

where $\left\langle J\left\|\hat{U}^{\lambda}\right\|J'\right\rangle$ is the double reduced matrix element. They are tabulated in Ref. [65].

The parentheses contain the $3j$ symbols, which are just another representation of the Clebsch-Gordan coefficients [36]; the function $\Xi(t,\lambda)$ is given by

$$\Xi(t,\lambda) = 2\sum_{n'l'}(2l+1)(2l'+1)(-1)^{l+l'} \times \begin{Bmatrix} 1 & \lambda & t \\ l & l' & l \end{Bmatrix}\begin{pmatrix} l & 1 & l' \\ 0 & 0 & 0 \end{pmatrix}\begin{pmatrix} l' & t & l \\ 0 & 0 & 0 \end{pmatrix}\frac{\langle nl|\, r\,|\, n'l'\rangle\langle nl|\, r^t\,|\, n'l'\rangle}{\Delta E_{n'l'}} \tag{1.23}$$

where $nl = 4f$, $n'l'$ is the excited configuration, while the summation runs over all allowed values of $n'$and l' of the excited configurations of opposite parity; the curly brackets contain the $6j$ symbol that relates the summation of three angular momenta [36,66]; $\Delta E_{n'l'}$ is the (average) energy of the excited configuration $n'l'$, $\langle nl\,|\,r\,|\,n'l'\rangle$; and $\langle nl\,|\,r^t\,|\,n'l'\rangle$ are the interconfiguration radial integrals:

$$\langle nl|\, r^t\,|\, n'l'\rangle = \int_0^{\infty} R(nl)r^t R(n'l')dr \tag{1.24}$$

Eq. (1.22) offers the possibility to estimate the transition dipole moment between any eigenstates of the ground configuration ($4f^N$). To this end, the radial integrals (Eq. 1.24) are computed, and then, the sums in Eqs. (1.22), (1.23) are carried out using the provided parameters of the (odd) crystal field A_{tp} and the average energy of the excited configuration $\Delta E_{n'l'}$.

Oscillator strength f for an electric dipole transition from the component i of the ground level to the component j of an excited level is defined as follows:

$$f = \chi\frac{8\pi^2 m\nu}{h}\left|\langle i|\,\hat{P}\,|j\rangle\right|^2 \tag{1.25}$$

where $\hat{P}$ is the electric dipole operator (Eq. 1.18), m is the mass of an electron, ν is the frequency of the spectral line, h is Planck's constant, and χ is the refractive index of the material in which the ion is embedded.

It is possible to evaluate the oscillator strengths in Eq. (1.25) by substituting the square of the transition dipole moment from Eq. (1.22). Nevertheless, the number

of parameters required is still quite large for practical applications. At this moment, Judd-Ofelt theory comes with a couple more approximations:

- All crystal-field states of the ground multiplet (denoted by i in Eq. 1.25) are equally populated. The error induced by this approximation is in direct relation with the splitting amplitude of the ground multiplet.
- Only the average over all Cartesian components is computed, that is, materials are considered optically isotropic.

Under these two approximations, the oscillator strength becomes

$$f = \chi \frac{8\pi^2 m\nu}{3h(2J+1)} \sum_{\lambda=2,4,6} \Omega_\lambda \left| \left\langle J \left\| \hat{U}^\lambda \right\| J' \right\rangle \right|^2 \tag{1.26}$$

where

$$\Omega_\lambda = (2\lambda+1) \sum_t \sum_p \frac{\left|A_{tp}\right|^2}{(2t+1)} \Xi^2(t,\lambda) \tag{1.27}$$

Developments of Judd-Ofelt theory were done in several directions:

- Including relativistic effects [67–70].
- Including the mixing between different J states. In some cases, this mixing is important for the ground multiplet, as pointed out in NIST data [35], and in calculations of complex spectra of free ions [71–76]. This addition to Judd-Ofelt theory [77] allowed to explain the electric dipole transitions occurring between two $J = 0$ states [78,79]. Note that such transitions are not allowed in the standard Judd-Ofelt theory.
- Including higher terms of electron correlation effects, beyond the single-configuration model, allowed to explain the origin of 0-0 and 0-1 transitions in Eu^{3+} ion in C_{2v}-symmetry hosts [80].
- Including covalent interactions between the metal and the ligand atoms [81].
- Including the explicit account for the spin-orbit coupling within excited configurations [82].

In practice, Judd-Ofelt theory is used to extract a set of phenomenological parameters Ω_λ from measured spectroscopic data that best describe Eq. (1.26). This allows to assign (some of the) measured spectroscopic lines to various $J \leftrightarrow J'$ electric dipole transitions. The success of Judd-Ofelt theory compared with other phenomenological models lies, in part, in the relatively small number of fitting parameters, while various approximations involved also allow for a certain degree of averaging of contributions for the computed values.

There have been some attempts to compute Judd-Ofelt parameters using the *ab initio* approach, but the results do not allow yet to make conclusions about the accuracy of their predictions [83,84].

1.3 Magnetism of lanthanide ions

Lanthanide ions entered the field of molecular magnetism with the discovery of $[Tb(pc)_2]^-$ anion [85,86], which was the first lanthanide-based single-ion magnet

[21,87]. Molecular magnets are molecules that are able to keep their own (intrinsic) magnetization for some time after the applied magnetic field is removed. When the magnetization blocking property is efficient, it leads to phenomena such as magnetic hysteresis, magnetic remanence, maxima in the out-of-phase magnetic susceptibility, and suppression of the low-temperature EPR signal [88]. Relative strong interest in molecular magnets was driven by the idea of storing information in an ultradense fashion—one bit per molecule (or atom)—provided that the surface of a hard drive was covered with molecular magnets in place of current materials.

Another important difference with the methods described above for the spectroscopic properties is that, since properties related to magnetism are usually detected at low temperatures, it is enough to consider the low-lying energy structure of lanthanide, that is, only the eigenstates of the $4f^N$ configuration are of major relevance [39].

1.3.1 Magnetic properties of free lanthanide ions

As inferred from Fig. 1.2, the effect of the applied magnetic field on the ground and excited J multiplets leads to their splitting in $2J+1$ nondegenerate components. The energy of the resulting eigenstates can be described as evolving linearly with the applied field:

$$E_m = M_J \mu_B g_J H \tag{1.28}$$

where M_J denotes the projection of the total momentum J on the direction of the applied field, μ_B is the Bohr magneton ($\mu_B = 0.4668643\,\mathrm{cm}^{-1}/\mathrm{T}$), g_J is the gyromagnetic factor for the ground J multiplet (which depends on all quantum numbers S, L, and J), and H is the strength of the applied field. The formula for g_J is [40]:

$$g_J = \frac{3}{2} - \frac{L(L+1) - S(S+1)}{2J(J+1)} \tag{1.29}$$

which considers gyromagnetic ratios of the orbital and spin momenta as $g_L = 1$ and $g_S = 2$, respectively.

Magnetization is a thermodynamic function that depends on the applied field and on temperature. The total magnetization of the system at a given temperature is a sum of the individual contributions of all states, weighted by their Boltzmann population factor. Van Vleck considered that the energy of individual states and the Boltzmann partition function can be broken into a Taylor (power) series w. r.t. applied field. He truncated both series at the second order and derived working expressions for magnetic susceptibility and magnetization [89]. The first derivative of the energy states (Eq. 1.28) with applied field is $E'_m = M_J \mu_B g_J$, independent of the strength of applied field. The second derivative is $E''_m = 0$. Setting the original $E_m = 0$ and substituting these results in the usual formula for Van Vleck's susceptibility give

$$\chi_m = \frac{N_A \sum_m \left(\frac{(E'_m)^2}{k_B T} - 2E''_m \right) e^{-\frac{E_m}{k_B T}}}{\sum_m e^{-\frac{E_m}{k_B T}}} = \frac{N_A \mu_B^2 g_J^2}{k_B T} \sum_{M_J} \left(\frac{(M_J)^2}{2J+1} \right)$$
$$= \frac{N_A \mu_B^2 g_J^2}{3 k_B T} J(J+1) \tag{1.30}$$

where N_A is the Avogadro number, k_B is the Boltzmann constant ($k_B = 0.6950356\ \mathrm{cm}^{-1}/\mathrm{K}$), and T is the temperature. It becomes clear now that the product of molar susceptibility is constant for a given multiplet (this is Curie's law for lanthanides):

$$\chi_m T = \frac{N_A \mu_B^2}{3 k_B} g_J^2 J(J+1) \approx 0.1250486\, g_J^2 J(J+1) \tag{1.31}$$

Table 1.4 shows the numerical values of $\chi_m T$ for all free lanthanide ions, for the variable number of states admixed by the spin-orbit. Note that spin-orbit coupling described in the basis of the ground J multiplet describes $\chi_{\mathrm{m}} T$ remarkably well.

In those cases in which the strength of the applied field H becomes comparable with $k_B T$, Curie's law is not valid, and the molar magnetization must be computed using the relation

$$M = \frac{N_A \sum_m \left(\frac{\partial E_m}{\partial H} \right) e^{-\frac{E_m}{k_B T}}}{\sum_m e^{-\frac{E_m}{k_B T}}} = N_A k_B T \left(\frac{\partial \ln Z}{\partial H} \right) \tag{1.32}$$

where $Z = \sum_m e^{-\frac{E_m}{k_B T}}$ is the partition function. In the particular case of $2J+1$ eigenstates arising from a given J multiplet, we have

$$Z = \sum_m e^{-\frac{E_m}{k_B T}} = \sum_m e^{-\frac{M_J \mu_B g_J H}{k_B T}} = \frac{\sinh\left[\frac{(2J+1)\mu_B g_J H}{2 k_B T} \right]}{\sinh\left[\frac{\mu_B g_J H}{2} \right]} \tag{1.33}$$

Substituting Eq. (1.33) in Eq. (1.32), after some transformation, we arrive at the following expression for the molar magnetization of free lanthanide ions:

$$M = N_A \mu_{\mathrm{B}} J g_{\mathrm{J}} B_J \left(\frac{g_J \mu_B J H}{k_B T} \right) \tag{1.34}$$

Table 1.4 High-temperature magnetic susceptibility data for free lanthanide ions, as a function of the quality of the spin-orbit coupling description (in $cm^3\,K\,mol^{-1}$)[a]

Ion	Ground config.	Total multiplicity	Ground term	Ground multiplet	XT computed within the ground multiplet only	XT (at 300 K) computed within the ground term only	XT (at 300 K) computed within the full $4f^N$ configuration
Ce^{3+}	$4f^1$	14	^2F	$^2F_{5/2}$	0.804	0.816	0.816
Pr^{3+}	$4f^2$	91	^3H	$^3H_4$	1.601	1.631	1.648
Nd^{3+}	$4f^3$	364	^4I	$^4I_{9/2}$	1.637	1.695	1.705
Pm^{3+}	$4f^4$	1001	^5I	$^5I_4$	0.900	1.014	1.008
Sm^{3+}	$4f^5$	2002	^6H	$^6H_{5/2}$	0.089	0.377	0.315
Eu^{3+}	$4f^6$	3003	^7F	$^7F_0$	0.000	1.634	1.308
Gd^{3+}	$4f^7$	3432	^8S	$^8S_{7/2}$	7.878	7.896	7.848
Tb^{3+}	$4f^8$	3003	^7F	$^7F_6$	11.817	11.880	11.779
Dy^{3+}	$4f^9$	2002	^6H	$^6H_{15/2}$	14.172	14.219	14.062
Ho^{3+}	$4f^{10}$	1001	^5I	$^5I_8$	14.068	14.099	13.936
Er^{3+}	$4f^{11}$	364	^4I	$^4I_{15/2}$	11.479	11.499	11.439
Tm^{3+}	$4f^{12}$	91	^3H	$^3H_6$	7.149	7.159	7.146
Yb^{3+}	$4f^{13}$	14	^2F	$^2F_{7/2}$	2.572	2.576	2.576

[a]Data were computed using the CASSCF/RASSI/SINGLE_ANISO method, an active space of CAS(N,7) and complete ANO-RCC basis [90,91]. Spin-orbit coupling was described within AMFI approximation [92,93].

where $B_J\left(\frac{g_J\mu_B JH}{k_B T}\right)$ is the Brillouin function for J multiplet, defined by

$$B_J(x) = \frac{2J+1}{2J}\coth\left[\frac{2J+1}{2J}x\right] - \frac{1}{2J}\coth\left[\frac{1}{2J}x\right] \tag{1.35}$$

The Brillouin function reaches unity for large values of applied field H, and the molar magnetization tends to its saturation value of

$$M = N_A\mu_B J g_J \tag{1.36}$$

In the case of real lanthanide-based compounds, these simple formulas may not work, since exact energies and their true field dependence are needed in Eq. (1.32), while the sum should eventually include all levels of the $4f^N$ configuration.

1.3.2 Ab initio *description of electronic structure and magnetism in lanthanide complexes*

Ab initio based methodologies made their way into the field of magnetochemistry several years ago. There are several reasons why this computational method is gradually taking over the traditional approaches used in this area. First, *ab initio* methods do not use fitting parameters, but rather use only the fundamental constants and physical laws, combined with rigorously chosen numerical approximations such that the ground and excited states of a given compound are computed only on the basis of the input molecular geometry. As such, *ab initio* methods allow for a systematic study of structure-property relationships. With respect to compounds containing lanthanide ions, a long-standing problem was the low-symmetry nature of the ligand environment, which required the full set of 27 crystal-field parameters to be fitted in a classical crystal field approach. This led to major overparameterization problems, given the impossibility of a reliable fit of such a large number of independent parameters. On the other hand, low symmetry of the molecular compound is not a problem for *ab initio* based methods, since the wave functions and their energies are derived self-consistently using the principle of minimization of the total energy. In this section, the *ab initio* based computational approach, which is now becoming a state of the art in the field of molecular magnetism, is described.

The large majority of *ab initio* electronic structure methods are currently based on the Born-Oppenheimer approximation, which allows separation of the electronic and nuclear motions, which also leads to the partition of the total wave function into a product of a pure nuclear wave function and a pure electronic wave function. The latter is of particular use, since it allows to solve a much simpler Hamiltonian only for the electronic eigenstates, keeping the nuclei fixed, unmoved. In other words, the nuclei positions enter as parameters in the electronic Hamiltonian.

The second approximation concerns the functional basis of the molecular Hamiltonian, that is, the choice of the basis set. This is a choice to be made by the researcher. Ideally, the basis set describing each atom should be sufficiently large, flexible

enough to be able to describe various changes of the shapes of the molecular orbitals due to covalence, polarization, and other effects arising from the interaction with other atoms. Within a chosen basis set, all electron repulsion integrals, core Hamiltonian, and other one-electron integrals (angular momentum, atomic-mean-field integrals for the spin-orbit coupling, relativistic corrections, etc.) are computed and used further in subsequent calculations. The union of all basis functions is also called atomic orbital (AO) basis, usually nonorthogonal. Any linear combination between atomic orbitals is called molecular orbital (MO) basis, usually orthogonal.

(1) *Complete-active-space self-consistent-field (CASSCF) method* is one of the core computational methods applied to lanthanide compounds. In this method, the orbital space is split in three sets: closed space (occupation=2), active space (occupation=fractional), and virtual space (occupation=0). Further, the wave function is represented as a linear combination between all Stater determinants arising from various distributions of the active electrons spanning the active orbitals. Closed and empty orbitals are not considered in this expansion. The CASSCF wave function is

$$|\psi\rangle_{CASSCF} = \sum_{I}^{Nr\ Conf} \cdot C_I |CSF\rangle_I \tag{1.37}$$

where C_I is configuration interaction expansion coefficients, while $|CSF\rangle_I$ is configuration state functions, that is, a linear combination between several Slater determinants with a given total spin.

The total energy minimization in the wave function deals with the simultaneous variation of the C_I coefficients and the coefficients of the molecular orbitals under the constraints that the sum of the squares of the C_I coefficients is normalized to unity and that all MOs remain orthonormal to each other. Explicit derivation of the CASSCF Lagrangian leads to the (coupled, second-order) Newton-Raphson equations. Their numerical implementation is not very efficient, and various simpler schemes have been designed such as, to mention a few, the decoupled form of the Newton-Raphson equations, with generally poor convergence issues, and the quasi-Newton method based on an augmented Hessian approach. Interested readers may find more information in the following sources [94–96].

Most of current implementations allow simultaneous optimization of several CASSCF wave functions in one calculation, as long as the same orbital basis is kept for all wave function expansions. This method is called state-average CASSCF method. This is the most popular method to be used in connection to lanthanide compounds, the reason being that this method gives a balanced description of the ground and of the excited states. In fact, all term eigenstates with a given total spin can be optimized within a single CASSCF calculation. In cases in which terms with several total spins exist for a given $4f^N$ configuration, then, several CASSCF calculations are needed to obtain all the necessary eigenstates.

Since the number of CSFs grows combinatorically with the size of the active space, the CASSCF method becomes intractable for active spaces larger than 16 electrons in 16 orbitals. In order to overcome this limitation, methods that impose various

limitations on the possible occupation of the active orbitals have been designed. Among them, one could mention the restricted-active-space self-consistent-field (RASSCF) [97] and the generalized-active-space self-consistent-field (GASSCF) methods [98–100]. The implementation of these methods in MOLCAS code [101] allows to expand the total active space up to some 25–28 electrons in the same number of orbitals.

Further expansion of the active space could be done using much different methodologies, based either on stochastic full configuration interaction quantum Monte Carlo (FCIQMC) [102] techniques or on density-matrix renormalization group (DMRG) methods [103–106], both allowing routine calculations of up to 40–60 active orbitals. However, these groups of methods have not been tested enough in connection with real lanthanide compounds to make a clear statement here about their performance.

(2) *Electron correlation methods*. The limitations of the CASSCF method are obvious. All active electrons are fully correlated, while excitations of core electrons are completely uncorrelated. In this respect, CASSCF wave function is just a slightly improved Hartree-Fock wave function, with the same issues of too large HOMO-LUMO energy gap and extralocalized orbitals. An obvious improvement over the CASSCF wave function is to gradually relax the drastic orbital occupancy limits imposed on the CASSCF wave function. One could design an improved wave function containing additional Slater determinants that possess some holes in the closed region and some electrons in the empty region. Evidently, the number of such Slater determinants grows extremely fast, and as a result, such methods quickly become prohibitively expensive for medium-to-large molecules.

There are two major ways of accounting for the effect of the excited configurations. First, there are the multistate multireference second-order perturbation theory methods like MS-CASPT2 [107–113] and MS-NEVPT2 [114,115]. Apart from the different zero-order Hamiltonian used in these two methods, they are pretty much similar, with comparable performance. With respect to free lanthanide ions, one drawback of both methods is the presence of artificial splittings, that is, small lifting of the exact degeneracy. The extended multistate version of the CASPT2 method (XMS-CASPT2) [116,117] performs much better compared with the original MS-CASPT2 version in this respect. To the best of the author's knowledge, there is no XMS version for the NEVPT2 method. Second, the methods based on the multistate multireference configuration interaction methods (MS-MRCI) [118,119] and various truncated versions of the same family exist and are waiting for their application in magnetochemistry. It has to be mentioned here that MRCI methods are significantly more expensive compared with the perturbative methods of equivalent excitation level.

(3) The account of the spin-orbit coupling is usually done in the second step. In this respect, the spin-orbit Hamiltonian matrix is built using the CASSCF/CASPT2 optimized eigenstates as basis [92,120,121]. The spin-orbit integrals for all elements are computed within the atomic-mean-field integral (AMFI) approach [93]. Diagonalization of the spin-orbit Hamiltonian written on the chosen basis of input states gives the spin-orbit eigenstates, which are further used to compute the matrix representation of the angular and spin momenta [92]. The latter are used in the computation of magnetic properties and for the determination of the parameters of pseudospin Hamiltonians (discussed below) and multiplet specific crystal-field splitting. Similar approaches are implemented in many quantum chemistry codes.

1.3.3 EPR g-tensor for lanthanide compounds

The combined effect of the low-symmetry crystal (ligand) field and the spin-orbit interaction leads to energy splitting of the eigenstates of the low-lying multiplet. It is usually not easy to predict the number of energy levels involved in the electron paramagnetic resonance measurements, since the splitting pattern depends only on the crystal environment. In such case, the experimental transitions and corresponding spectra are interpreted with the help of an effective spin (pseudospin) Hamiltonian of the form [40,89,122]:

$$H = \mu_B \boldsymbol{g} \widetilde{S} H + \widetilde{S} \boldsymbol{D} \widetilde{S} \tag{1.38}$$

where the first term specifies the Zeeman interaction and the second term accounts for the zero-field splitting effect; $\boldsymbol{g}$ and $\boldsymbol{D}$ are 3×3 symmetrical tensors, while $\widetilde{S}$ is the pseudospin, having the dimension equal to the number of low-lying spin-orbit eigenstates. The second term ($\widetilde{S}\boldsymbol{D}\widetilde{S}$) in Eq. (1.38) is only present for cases when $\widetilde{S} \geq 1$. For pseudospins with a dimension larger than one, higher-rank operators for the Zeeman splitting and for zero-field splitting must be included [56,123,124].

As an example, consider Dy^{3+} ion in some low-symmetry ligand field environment. The orbital momenta $L = 5$ and spin momenta $S = 5/2$ of the ground multiplet are not good quantum numbers, as they are coupled by the spin-orbit interaction. The total angular J is again not a good quantum number, since it is split by the ligand field. As a result, the EPR measurement may only detect transitions occurring between the two components of the ground Kramers doublet. Thus, a pseudospin $\widetilde{S} = 1/2$ in Eq. (1.38) is the most appropriate in this case.

Another example deals with the partial removal of the $2J+1$ degeneracy of the free ion, due to relatively high symmetry of the ligand field. In this case, let us consider Nd^{3+} ion in some rigorous octahedral crystal-field environment [123]. The ground $J = 9/2$ is split in this ligand environment in two Γ_8 and one Γ_6 in the octahedral double group. The ground state is a Γ_8 state—a group of four spin-orbit states with exactly the same energy. Clearly, in any EPR measurement, various transitions between all these four states will be detected. Therefore, the most appropriate pseudospin in this case is $\widetilde{S} = 3/2$.

Diagonalization of the $\boldsymbol{g}$ tensor in Eq. (1.38) gives the main values (g_x, g_y, and g_z) and three eigenvectors—the *main magnetic axes*. Typically, the largest value is assigned to g_z, the smallest to the g_x and the intermediate value to g_y. The main magnetic axes form a right-handed coordinate system. The system is said to be *anisotropic* whenever $g_x \neq g_y \neq g_z$. Lanthanide ions, due to their large unquenched orbital moment in the ground state, have a strong potential to display strong magnetic anisotropy in the ground and excited states. The limit of magnetic anisotropy is the Ising anisotropy (pure axial anisotropy), $g_x \neq g_y \neq 0$, while $g_z \neq 0$. Investigation of pure Ising anisotropy by EPR is not possible because the transition between the two components of an Ising doublet is forbidden.

Diagonalization of the $\boldsymbol{D}$ tensor in Eq. (1.38) gives the main values as D_x, D_y, and D_z and three eigenvectors—the *main anisotropy axes*. It must be emphasized here that there is no relationship between the main magnetic and the main anisotropy axes, implying that 12 independent parameters are needed to describe Eq. (1.38). In practice, in order to avoid overparameterization issues, the main magnetic axes and main anisotropy axes are considered parallel to each other, which are not justified for low-symmetry systems.

The questions of how to relate *ab initio* spin-orbit eigenstates and the pseudospin eigenstates (i.e., states with a well-defined momentum on the quantization axis) and how to find the orientation of the most appropriate quantization axis w.r.t. the initial coordinate system were considered in detail by Chibotaru [124]. In particular, the procedure of determination of the parameters of the crystal field from the *ab initio* calculations uses the concept of pseudospin, generalized to the pseudo-J formalism [57].

In MOLCAS [101] and MOLPRO [125] *ab initio* quantum chemistry packages, the computation of static magnetic properties using the *ab initio* results is done by the SINGLE_ANISO program [56,126]. Details on the implemented formulas were given in Ref. [127]. This program is able to compute the parameters of the pseudospin Hamiltonians (g tensor, D tensor, and higher-rank pseudospin operators), the parameters of the crystal field for lanthanides, the thermodynamic functions for the temperature-dependent magnetic susceptibility tensor, the powder molar susceptibility, the field- and temperature-dependent molar magnetization, and the magnetization vectors. An approach to plot the blocking barrier for molecular magnets was proposed [128] and used in many studies [22,129–132].

1.3.4 Magnetic susceptibility and molar magnetization as a function of the size of the spin-orbit coupled basis

General equations were derived on the basis of Van Vleck's theory for the molar magnetization and magnetic susceptibility and implemented in SINGLE_ANISO code. The exact expressions are given in Ref. [127]. In this section, the accuracy of the computation of the magnetic susceptibility as a function of the quality of the description of the spin-orbit interaction is analyzed. The first tabulation of XT data dates to Van Vleck, who computed the values of the molar magnetic susceptibility for free lanthanide ions considering the eigenstates of the ground multiplet only [133]. In the model of ground multiplet only, temperature population of excited multiplets is neglected, as well as their weak admixture to the wave functions of the ground multiplet. Here, one is able to compare these results with the cases when the spin-orbit coupling is described better: (*i*) by considering all multiplets originating from the ground term and (*ii*) by considering all terms arising from the $4f^N$ configuration. A further improvement would be to account for the influence of the excited configurations, like $4f^{N-1}5d^1$ and $4f^{N-1}6s^1$. This task is left for the future. Table 1.4 shows the results obtained from these benchmark calculations.

Analyzing the XT data in Table 1.4, one could mention the following trends for the high-temperature magnetic susceptibility as a function of the quality of the description of the spin-orbit coupling.

For lanthanide ions with less-than-half-filled 4*f* shell (Ce^{3+}-Eu^{3+}), magnetic susceptibility generally increases compared with the predicted susceptibility on the basis of ground multiplet. The difference between the susceptibility computed in the full basis of the 4*f* eigenstates and the one computed in the truncated basis of the ground multiplet ranges from 0.01 for Ce^{3+} to 0.3 for Sm^{3+}, with a sharp maximum of 1.3 for Eu^{3+} (Table 1.4). The latter value is a sign of a remarkably strong temperature-independent paramagnetism (TIP) effect for Eu^{3+} [89,134], originating from Boltzmann population of the relatively low-lying excited magnetic multiplets at room temperature. The strong TIP of Eu^{3+} ions in complexes is preserved, since the crystal-field effect does not usually change much the relative position of the gravity center of free-ion multiplets.

For lanthanide ions with more-than-half-filled 4*f* shell (Tb^{3+}-Tm^{3+}), the trend is the opposite and less pronounced. Magnetic susceptibility described in the full basis of 4*f* eigenstates is slightly smaller compared to the theoretical value predicted for the ground multiplet. The largest deviation is attested for Dy^{3+} (−0.11) and Ho^{3+}(−0.13). For Gd^{3+} and Yb^{3+}, the differences are rather negligible.

To a lesser extent, the above described trends are also valid for the molar magnetization.

In all cases, the crystal-field effect induces further mixing between energy levels of the ground and excited multiplets. To some extent, the crystal-field splitting of the ground *J* multiplet will cause a reduction of *XT* compared to the free-ion data, while the stronger admixture of the excited *J* multiplets (induced by the crystal-field splitting) will enhance the above discussed trends. Therefore, it is recommended to describe the spin-orbit coupling and magnetic properties using the *complete* $4f^N$ as a basis.

1.3.5 Strong magnetic anisotropy and magnetization blocking of lanthanide ions

Lanthanide ions currently hold leadership in the design of novel single-molecule magnets [11,12,14,23,135–139]. The top-performant molecular magnets to date are based on—or include as important ingredients—lanthanide ions. The reason why lanthanide ions have taken over transition metals is their much larger total momentum, which allows relatively large splitting in common chemical compounds. The effect of the crystal environment leads, in certain cases, to strong (axial) magnetic anisotropy in the ground and excited states [22,140]. The application of a magnetic field to a strongly anisotropic compound orients all the magnetic moments of all molecules in the crystal along the magnetic field (i.e., along their intrinsic g_z magnetization axis, toward a minimum angle with the applied field). An efficient molecular magnet (single-molecule magnet, SMM) is a complex molecule that is able to retain its own magnetized state for a long time after the magnetic field is removed, at reasonably high temperatures. Fig. 1.4 shows an optimal structure of the low-lying doublet states of a molecular magnet, on the example of the best predicted SMM—the DyO^+ [128,139]. At low temperatures, only the ground state $|\pm n\rangle$ is populated. Application of an external magnetic field leads to the population of only one component, for

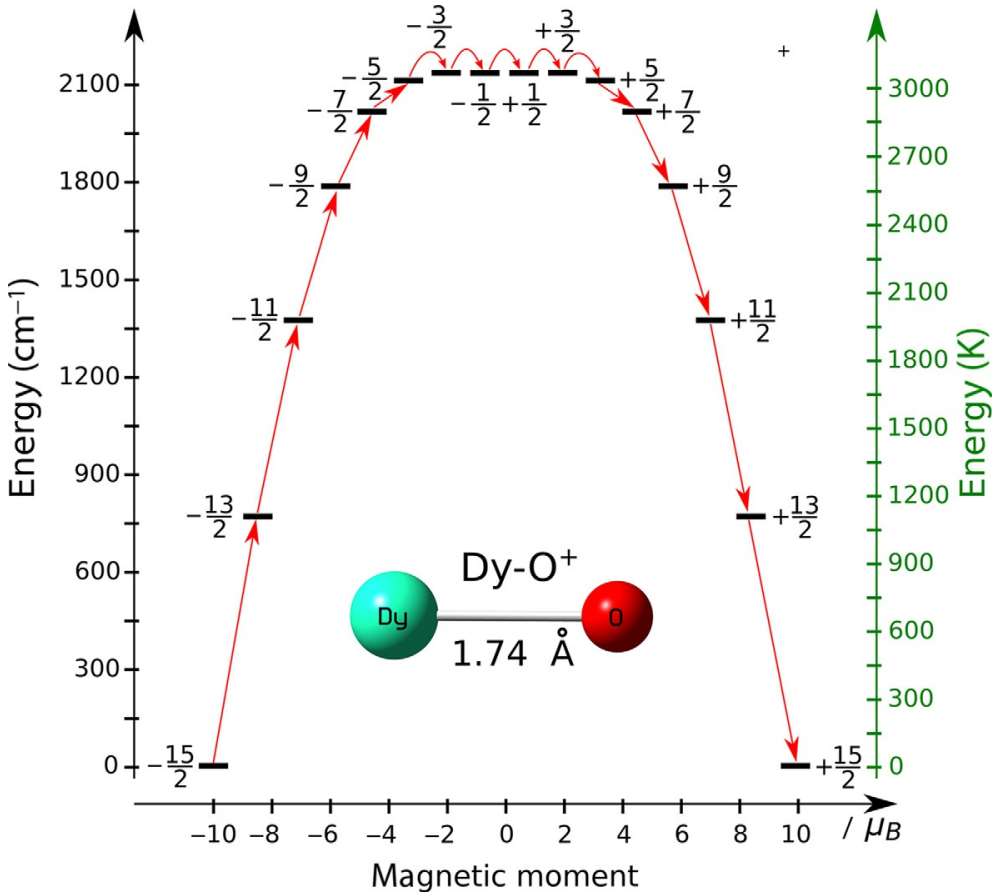

Fig. 1.4 Scheme of the low-lying spin-orbit states ($\pm n$) corresponding to the crystal-field components of the ground-state atomic J multiplet in DyO^+ cation [128]. This is an example of an ideal SMM, where all relaxation channels are suppressed, except the ones displayed by *red arrows*. Less efficient (i.e., less axial) molecular magnets contain significant values of the transition matrix elements of the magnetic dipole and/or spin-phonon interaction between various states, for example, $-\frac{15}{2} \rightarrow +\frac{15}{2}$,$-\frac{15}{2} \rightarrow +\frac{13}{2}$, $-\frac{15}{2} \rightarrow +\frac{11}{2}$, $-\frac{13}{2} \rightarrow +\frac{13}{2}$, and $-\frac{13}{2} \rightarrow +\frac{11}{2}$, opening new relaxation pathways that lead to lower barrier heights, stronger quantum tunneling, and faster magnetic relaxation.

example, $|+n\rangle$. In the absence of the applied magnetic field, the energy of the two components becomes the same, and therefore, transition between the two components $|+n\rangle$ and $|-n\rangle$ may occur. Magnetic relaxation refers to the dynamic process of equalizing the populations of the two components of the ground $|\pm n\rangle$ doublet. At low temperatures, the necessary condition for the blocking of magnetization is that the rate of the flipping of magnetization via quantum tunneling of magnetization (QTM) process between components of the ground doublet $|+n\rangle \leftrightarrow |-n\rangle$ is small [21]. At larger temperatures, two other relaxation mechanisms contribute to magnetic relaxation: Raman and Orbach processes. Both of them involve absorption and emission of phonons via spin-phonon interaction. At temperatures at which the first excited doublet acquires population, temperature-assisted QTM process starts to contribute. The lowest doublet state at which intensive magnetic relaxation occurs defines the height of

the blocking barrier U_{eff} in the activation mechanism of relaxation. This mechanism becomes dominant at relatively high temperatures, at which its rate exceeds the rates of other processes (e.g., QTM): $\tau^{-1} = \tau_0^{-1} e^{\left(-\frac{U_{\text{eff}}}{kT}\right)}$ [87,141,142].

An efficient SMM is characterized by a large multistep activation barrier (U_{eff}), involving as many doublet states as possible or as contained in the ground J multiplet. This status is achieved in cases in which all transitions related to unwanted relaxation processes between low-lying spin-orbit states are suppressed.

In common Ln^{3+} compounds, the low-lying states mostly originate from the crystal-field splitting of the ground J multiplet [42]. Their wave functions can be written as

$$|n\rangle = \sum_{m=-J}^{J} c_{nm} |Jm\rangle \tag{1.39}$$

The wave function of the state with magnetization in the opposite direction is obtained by applying the time-reversal operator θ to the state $|n\rangle$:

$$|-n\rangle = \theta|n\rangle = \sum_{m'=-J}^{J} (-1)^{J+m'} c^*_{n-m'} |Jm'\rangle \tag{1.40}$$

where the m and m' are projections of the total momentum J on some quantization axis, while coefficients c_{nm} are obtained by the diagonalization of the crystal-field operator:

$$\widehat{H}_{CF} = \sum_{k} \sum_{q=-k}^{k} B_{kq} O_k^q(J) \tag{1.41}$$

where B_{kq} is parameters of the crystal field and $O_k^q(J)$ is even-rank Stevens (complex) operators of rank k and projection q for the J multiplet [40].

As discussed above, the dominant relaxation processes are mediated by the interactions between magnetic moments of the molecules and phonons (organized vibrations of all atoms in the crystal/surface) [21]. The electron-vibrational operator, inducing transitions between low-lying doublets (Fig. 1.4), is similar in its structure to Eq. (1.41), with the difference that the parameters of the crystal field depend on the distortion modes involved in the corresponding phonon states, $b_{kq} = \partial B_{kq}/\partial q_i$. A general form of the electronic transition matrix elements between doublet states with opposite magnetization can be expressed as

$$\langle -n | b_{kq} O_k^q(J) | n' \rangle = \frac{b_{kq}}{p_k} \langle J \| O_k \| J \rangle \times \sum_{m=-J}^{+J} \sum_{m'=-J}^{+J} (-1)^{J+m} c_{n-m} c_{n'm'} C^{Jm}_{kqJm'} \tag{1.42}$$

where the reduced matrix element $\langle J\|O_k\|J\rangle$ and the proportionality coefficients p_k are defined in Ref. [56], while $C^{Jm}_{kqJm'}$ is the Clebsch-Gordan coefficient [36]. The term on the right-hand side of Eq. (1.42) becomes zero whenever the Clebsch-Gordan coefficient is zero, that is, when $m+m' \neq q$. Since the maximum value of the projection q of the Stevens operators in Eq. (1.41) is bound to ± 6, while the dimension of the ground multiplet J for many lanthanides offers more freedom (e.g., ± 8 for Ho^{3+}, ± 7.5 for Dy^{3+} and Er^{3+}), it must be possible to design such wave functions in the low-lying doublets where the spin-phonon transition is completely blocked. This is achieved whenever the difference between projections m (entering the wave function of $\langle -n|$) and m' (entering the wave function of $|n'\rangle$) is large. In practice, this is achieved for an axial (linear) crystal field, where $|\pm n\rangle$ states are of almost pure $|J,\pm|m|\rangle$ character. Fig. 1.4 shows an example for the best predicted Ln-based molecular magnet.

The importance of the $b_{kq}O^q_k(J)$ individual components of the spin-phonon transition operators in Eq. (1.42) depends on the actual change in the magnetic structure induced by vibrations [87,143,144]. For pure spin molecular magnets (e.g., $Mn_{12}Ac$), the dominant term in the spin-phonon transition is the rotation of the main anisotropy axis of the ground doublet induced by vibrations. The corresponding spin-phonon operators take the form of an anticommutator, proportional to $\{S_{x,y},S_z\}$, where z is the main anisotropy axis. In lanthanide systems, the "rotational" contribution to the spin-phonon transition (of the form $\sim\{J_{x,y},J_z\}$) is expected to be dominant as well [145,146].

Magnetic relaxation at very low temperatures, at which only the ground state is populated, is dominated by QTM, while its rate scales as the square of the tunneling gap Δ^2_{tun} [147,148]. The latter is defined as the energy difference between the two components of the ground doublet. The tunneling gap can be of *intrinsic* origin—for systems with an even number of electrons—or *induced* via a Zeeman splitting, in complexes with an odd number of electrons ($2\Delta_{tun} = \mu_B\sqrt{g_x^2H_x^2 + g_y^2H_y^2}$, where $g_{x,y}$ is the components of the $\boldsymbol{g}$ tensor in the transversal directions to the main anisotropy axis and $H_{x,y}$ is the respective components of the magnetic field).

Axiality of a doublet is defined as the smallness of the tunneling gap [128]. The necessary condition for SMM behavior is a high axiality of the ground doublet:

$$\Delta_{int} = \left\langle -n\middle|\,\widehat{H}_{CF}\middle|+n\right\rangle \tag{1.43}$$

$$\mu_{x,y} = 2\left\langle -n\middle|\,\hat{\mu}_{x,y}\middle|+n\right\rangle/\mu_B$$

where magnetic moment acquires a simple form $\mu = -g_J\mu_B\boldsymbol{J}$, with matrix elements similar in structure to Eq. (1.42) ($J_\alpha \sim O^\alpha_1$) [36]; therefore, all arguments given there for the suppression of the spin-phonon matrix elements are applicable here as well. In particular, for large differences between projections of the J moment entering in the expansion of $\langle -n|$ and $|n\rangle$ (Eqs. 1.40, 1.41), the quantities in Eq. (1.43) are suppressed. This is achieved, for example, when axial components of the crystal field in Eq. (1.42) (B_{20}, B_{40}, and B_{60}) significantly exceed the effect of the nonaxial components (B_{2q}, B_{4q}, B_{6q}, and $q \neq 0$). Such a situation leads to a strong axial character of the wave functions of the ground doublets, $|\pm n\rangle \approx |J,\pm|m|\rangle$.

The Ising character of the doublet functions permits one to reduce the transition matrix elements of the "rotational" contribution to the electron-vibrational interaction, $\sim\{J_{x,y},J_z\}$, to the matrix element of the corresponding $J_{x,y}$ (or $\mu_{x,y}$). The average matrix element of the spin-phonon transition can be written as [128,129]:

$$\overline{\mu}_{-n,n'} = \frac{1}{3}\left(|\langle -n|\,\mu_x|n'\rangle| + \left|\langle -n|\,\mu_y|n'\rangle\right| + |\langle -n|\,\mu_z|n'\rangle|\right) \tag{1.44}$$

The spin-phonon transition scales as a square of $\overline{\mu}_{-n,n'}$. This allows to assess the relative importance of relaxation paths between various states and to understand the structure of the relaxation barrier [129,149,150]. In the case of a perfectly axial crystal field (all B_{2q}, B_{4q}, B_{6q}, and $q \neq 0$ are zero), the wave functions of the ground J multiplet have pure $|J, \pm|m|\rangle$ character. As an example, libration- and rotation-type nuclear motions induce spin-phonon transitions in linear (axial) molecules, such as DyO^+. Indeed, Eq. (1.44) shows that only transitions between states differing by $\Delta m = \pm 1$ are allowed. Fig. 1.4 shows the resulting blocking barrier for this cation.

Perfect magnetic axiality may be induced by symmetry. For example, a doublet is perfectly axial ($g_\perp = 0$) only if the irreducible representation $E_\perp$, after which the two transversal components of the magnetic moment transform (denoted by E, E_1, or E′ in different symmetry groups), is not contained in the symmetrized square of the irreducible representation E_{KD} after which this Kramers doublet transforms, $E_\perp \notin [E_{KD}^2]$. Table 2 in Ref. [128] lists all possible cases in which perfect axiality for Kramers doublets and for Ising doublets is achieved. We have investigated by *ab initio* methods the influence of coordination number and geometry on the nature of the ground state of a hypothetical $[DyF_n]^{3-n}$ anion series (at $R = 2.5$ Å). The obtained crystal-field splitting and the dominant component of the projection of the total momentum J on the quantization axis are shown in Fig. 1.5. The results show clearly that low coordination numbers give the largest crystal-field splitting (and magnetic axiality). Conversely, the closer the distribution of the surrounding ligands to the spherical symmetry is (i.e., large coordination numbers and high symmetry), the smaller the crystal-field splitting is. The lack of magnetic anisotropy is attested for icosahedral, octahedral, cubic, and tetrahedral point-group symmetries.

The performed *ab initio* calculations (without employing any symmetry constraints) have shown that low-symmetry Ln^{3+} ions and fragments may also display strong magnetic anisotropy (axiality) for a few excited doublet states. The main magnetic axes in excited doublet states may be rotated with respect to the main axis of the ground doublet state, sometimes with rotations in the order of several tens of degrees. This fact underlies a major mechanism for spin-phonon transitions between axial doublets. To understand this, one needs to rotate the wave function of the excited doublets to be collinear with the quantization of the ground doublet. Some of the coefficients of decomposition with small difference of projections ($m-m'$, see Eq. 1.42) of the rotated wave function are strongly dependent on the rotation angle. These coefficients quickly increase with the rotation angle between the states, explaining why the spin-phonon process becomes operative in such doublet state. Indeed, in most mononuclear lanthanide compounds, the relaxation barrier corresponds to the energy of the first excited doublet state. Indeed, because of the large angle between magnetic axes in the ground

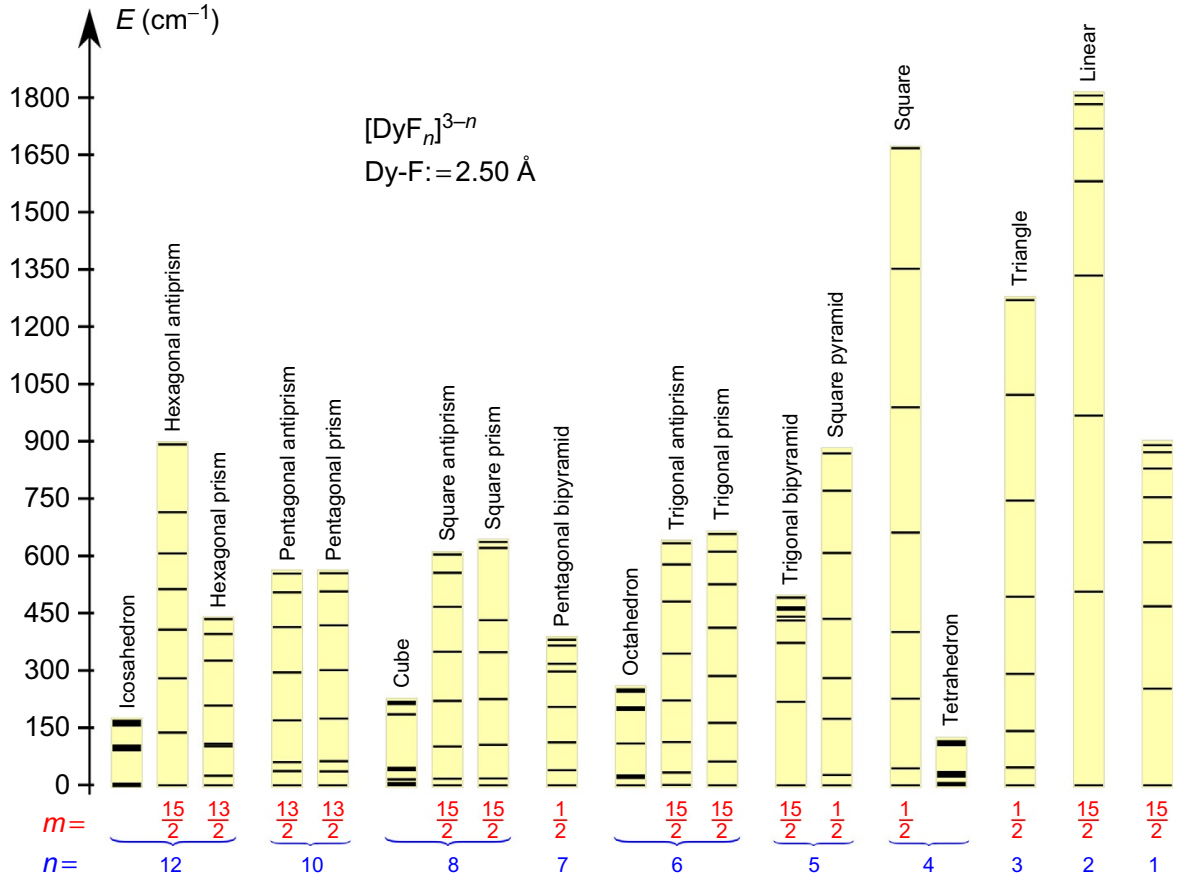

Fig. 1.5 Structure of low-lying Kramers doublets of the $J = 15/2$ ground-state multiplet of hypothetical $[DyF_n]^{3-n}$ complexes of Dy^{3+}, calculated by *ab initio* methods for various coordination geometries at an arbitrary fixed Dy-F distance (2.50 Å). The coordination numbers n are given at the bottom. m indicates the projection of the total angular momenta J in the ground KD state. For the icosahedron, cube, and tetrahedron, the ground state is Γ_8 (fourfold degenerate), and it is magnetically isotropic (i.e., with no preferred orientation of magnetization). The ground doublet state of the octahedral structure is an isotropic Kramers doublet.

and excited states, there will be relaxation of the Orbach and Raman types between them. In the presence of strong/dominant axial crystal-field components, the angle between ground and excited doublets is small, thus suppressing the spin-phonon relaxation. In fact, lanthanide-based molecular magnets with relaxation barrier corresponding to the second [149,151], third [152], and even fourth excited Kramers doublets [137,153,154] have been identified in real compounds.

Electronic density of free lanthanide ions with definite projection of the total momentum J on a given axis is symmetrical w.r.t. rotation around that axis. It depends nonmonotonically on the nature of the lanthanide ion and on the specific J eigenstate [155]. Decomposition of the electronic density of the 4*f* electrons up to second rank (up to quadrupole moment) gives an ellipsoid of rotation, either *prolate* (axially elongated) or *oblate* (expanded at equator) [156]. Within such a simplified description, it is possible to correctly explain the stabilization of $|Jm\rangle$ states of Ln^{3+} ions in environments with dominant axial and/or equatorial components of the crystal field.

For example, Dy^{3+} ion has a prolate electronic density in the $\left|\frac{15}{2}, \pm\frac{1}{2}\right\rangle$ doublet state and an oblate density in the $\left|\frac{15}{2}, \pm\frac{15}{2}\right\rangle$ doublet. The latter doublet is stabilized by an axial crystal field, while the former is stabilized by an equatorial field, clearly confirmed by the *ab initio* computed data in Fig. 1.5. The situation is rather different in the case of Er^{3+} ion: electronic density is prolate in the $\left|\frac{15}{2}, \pm\frac{15}{2}\right\rangle$ state and oblate in the $\left|\frac{15}{2}, \pm\frac{1}{2}\right\rangle$ state. The latter is stabilized by an axial ligand field, while the former is stabilized by an equatorial ligand field, opposite to the situation described for Dy^{3+} ion.

In order to understand the factors underlying the drastic differences in the stabilization of the ground-state crystal-field multiplet in Dy^{3+} and Er^{3+} complexes, Fig. 1.6 shows the orbital structure of the $\left|\frac{15}{2}, \pm\frac{15}{2}\right\rangle$ state for both ions in an axial ligand field. Comparing the plots in Fig. 1.6B and C, one can note that the two additional spin-down electrons in Er^{3+} occupy the orbitals that are most destabilized in axial ligand fields ($m_l = 1$ and 0).

This destabilization is produced by stronger covalent [57] and electrostatic interactions of these orbitals with the ligand ones because of their elongation in the axial direction (Fig. 1.6D) [157]. As a consequence of this, the energy destabilization of the orbitals with $m_l = 1$ and 0 is the fundamental reason why the axial fields stabilize the $\left|\frac{15}{2}, \pm\frac{15}{2}\right\rangle$ state of the Dy^{3+} and destabilize the analogous state in Er^{3+}.

On the basis of the above considerations, confirmed by rigorous *ab initio* calculations, it was theoretically predicted [158] that $[Er(COT)_2]^-$ anion (COT^{2-} = cyclooctatetraene anion) would block the magnetization much better than its Dy^{3+} analogue. This prediction achieved experimental confirmation [132,159]. Fig. 1.7 shows a comparison between the magnetic hysteresis curves of the Dy and Er anions (Fig. 1.7A and B) and their *ab initio* computed blocking barriers (Fig. 1.7C and D).

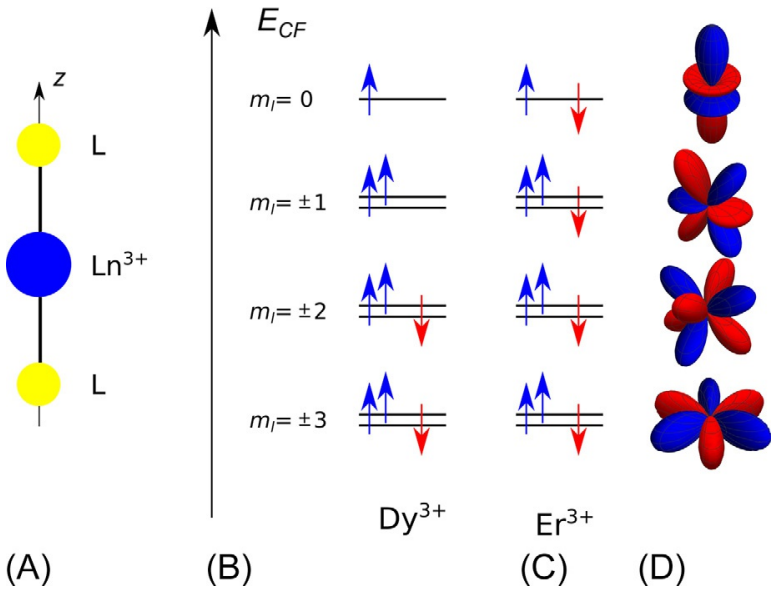

Fig. 1.6 Orbital structure of the $\left|\frac{15}{2}, \frac{15}{2}\right\rangle$ state of Dy^{3+} (B) and Er^{3+} (C) ions in a pure axial CF (A). The energy levels correspond to seven atomic 4*f* orbitals that are split into three orbital doublets in an axial field, with the projection of the electronic orbital momentum *l* on the CF axis $m_l = \pm 3$, ± 2, and ± 1, and one orbital singlet with $m_l = 0$. The plots in part (D) show a real combination of the corresponding $\pm|m_l|$ orbitals. In contrast to them, the density of complex m_l orbitals is invariant with respect to rotations around *z*.

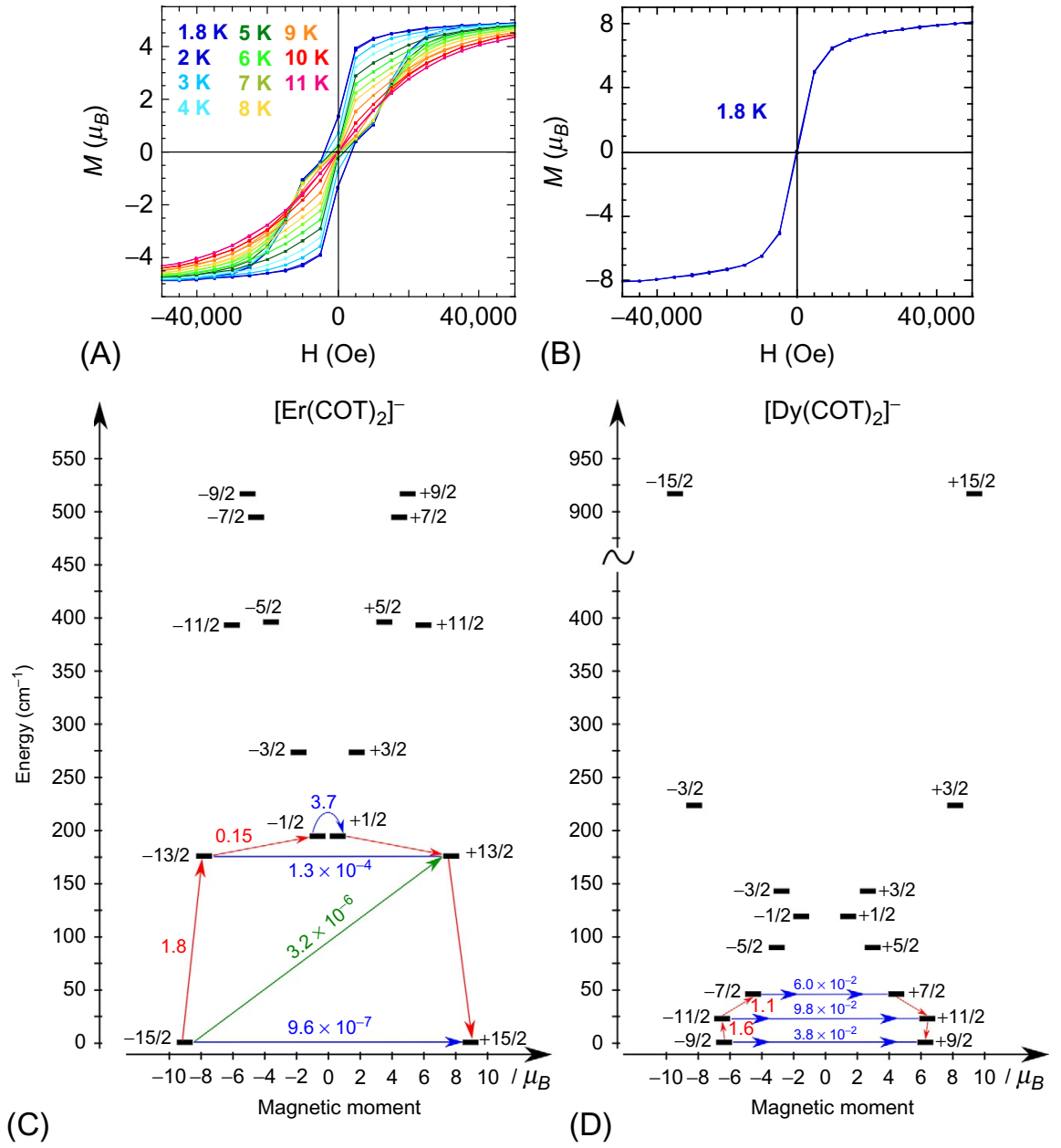

Fig. 1.7 (A) Magnetization hysteresis loops for $[Er(COT)_2]^-$ anion measured on a SQUID at 35 Oe/s sweep rate at indicated temperatures. At $T = 1.8$ K, the coercivity (distance between $M(H)$ points at $M = 0$) is ca. 7000 Oe. (B) Equivalent measurement for $[Dy(COT)_2]^-$ at 1.8 K. (C) The magnetization blocking barriers in $[Er(COT)_2]^-$ (A) and $[Dy(COT)_2]^-$ (B) compounds. The thick black lines represent the Kramers doublets as a function of their magnetic moment along the axis connecting the centers of COT rings. The *green dashed lines* correspond to diagonal quantum tunneling of magnetization (QTM); the *blue dashed lines* represent Orbach relaxation processes. The numbers next to each *arrow* stand for the mean absolute value of the corresponding matrix element of transition magnetic moment $((|\mu_X|+|\mu_Y|+|\mu_Z|)/3)$. The path shown by the *red arrows* represents the most probable path for magnetic relaxation in the corresponding compounds.

An interesting effect that can be mentioned here is that oblate ions display a significantly larger crystal-field splitting compared with prolate ones in an identical crystal-field environment. For example, $[Dy(COT)_2]^-$ anion shows a crystal-field splitting twice larger than that of $[Er(COT)_2]^-$ analogue compound. These differences between the properties of the ground J multiplet of Dy^{3+} and Er^{3+} ions are related to the opposite signs of the Stevens α and β parameters, which are larger for Dy^{3+} and of opposite sign [39,40].

Thus, a few advices on how to design better molecular magnets based on lanthanide ions are as follows:

- Use oblate lanthanide ions (Dy^{3+}, Tb^{3+}, and, to a lesser extent, Ho^{3+}), since they offer the highest blocking barriers (due to larger crystal-field splittings).
- Effectively lower the coordination number. This means that the chemical design of a novel molecular magnet should attempt to obtain a strong chemical bond between the Ln^{3+} ion and one ligand atom (or two ligand atoms, at opposite sides). At the same time, all other chemical bonds should be as weak as possible, to avoid perturbing the magnetic axiality induced by the designed short chemical bond. In this way, the effective coordination number approaches the axial limit.
- Attempt to obtain two-coordinate or linear compounds, provided that equatorially bonded ligand atoms destroy the axiality in a drastic manner [130,139,160] and that their removal from the coordination environment leaves the dominant axial ligand field as the only source of perturbation.
- Deposit or store the strong magnetic units, such as DyX, TbX, or HoX (where X = F, Cl, O, etc.), on a surface or on top of or inside some material. The condition here is that the surface or the host material leads to a weaker interaction to the Dy site than the bonded oxygen, such that the dominant contribution of the latter is preserved as close as possible to the gas-phase situation.

Fig. 1.8 shows that the blocking barrier of the deposited or the hosted DyO^+ unit is significantly larger compared with the blocking barrier displayed by the deposited free Dy^{3+} ion.

To date, oblate lanthanide ions (in particular, Dy^{3+}) keep current records for the performance of magnetization blocking behavior. The current top-performant single-ion magnet is the $[Dy(cp)_2]^+$ cation, which displays magnetic hysteresis at nearly 60 K, with a calculated height of the activation barrier of 1800 cm^{-1} [137,153], thus approaching the predicted theoretical limit of ~2100 cm^{-1} for DyO^+ (Fig. 1.4). Among other recently reported single-ion magnets, one can mention Dy in nearly D_{5h} symmetry, [130,131,161,162], a nearly linear Dy compound [150], a diamide Dy compound [163], etc.

1.3.6 *Accuracy of the* ab initio *methodology for the prediction of the electronic structure and properties of lanthanide systems: Er-trensal case*

The accuracy of the predicted crystal-field splitting is strongly dependent on the quality of the performed calculations. *Ab initio* computational methods can be improved on a rigorous basis (i.e., systematically) by increasing the level of computational

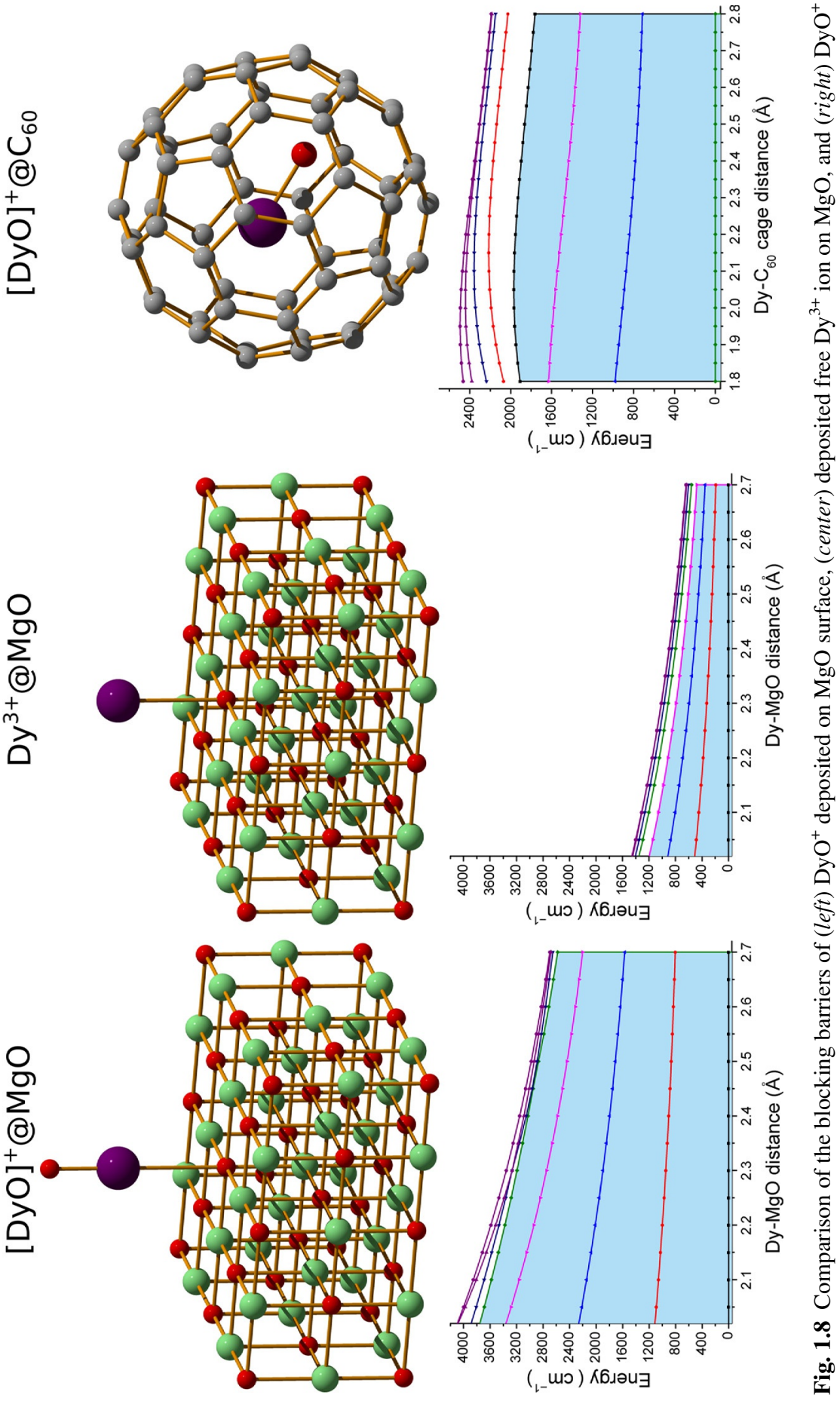

Fig. 1.8 Comparison of the blocking barriers of (*left*) DyO^+ deposited on MgO surface, (*center*) deposited free Dy^{3+} ion on MgO, and (*right*) DyO^+ hosted inside a neutral fullerene.

description of the wave function. This property underlines a clear advantage of these methods over phenomenological models (e.g., PCM), semiempirical quantum chemistry approaches, and methods based on density functional theory (DFT). The computational method based on state-average CASSCF/SO-RASSI/SINGLE_ANISO described in Section 1.3.2 proved a reliable and reasonably accurate tool for the description of the electronic structure and magnetism of a large number of lanthanide-based complexes [22]. This computational strategy could be systematically improved (*i*) by considering larger basis sets describing individual atoms in the investigated compound, (*ii*) by considering a larger active space for the CASSCF method, (*iii*) by including the dynamic electronic correlation (the CASPT2 step), (*iv*) by describing the spin-orbit coupling at a better level (e.g., by mixing more spin states within the spin-orbit interaction), (*v*) by accurately describing the electrostatic Madelung and other long-range effects of the environment, and (*vi*) by lowering the thresholds (increasing the integration grids) for various integral evaluation and/or density-fitting algorithms and tightening the numerical convergence of the *ab initio* calculations. Such increase of the computational level is particularly important for the accurate evaluation of the entire crystal-field spectrum. Indeed, the CASSCF/RASSI is usually sufficient for a reasonable description of the ground and low-lying crystal-field states (mostly responsible for the magnetism), while it can often underestimate the energies of the excited crystal-field states. The accuracy of prediction of excited terms could be also improved.

Clearly, a complete benchmark of all abovementioned effects is needed. Here, the effects of the size of the active space, of the dynamic electron correlation, and of the Madelung potential on the predictions of the crystal field are discussed on the basis of the recently investigated trigonal Er-trensal molecule [57,164]. For this compound, the CASSCF/RASSI computational approach proved to be insufficiently accurate for the description of magnetic properties and crystal-field spectrum for the excited four crystal-field levels. It must be mentioned here that Er-trensal was thoroughly investigated by experimental means. Low-lying energy spectra were extracted from luminescence measurements [165,166], and a few of the transitions received further confirmation from inelastic neutron scattering (INS) investigation [164]. Magnetic properties of this compound were probed by single-crystal magnetic measurements, while *g* tensor in the ground doublet state received additional confirmation from an electron paramagnetic resonance (EPR) study.

All calculations shown in this section were performed using MOLCAS quantum chemistry package [101] and were based on the experimental structure of the Er-trensal complex, determined at room temperature. Er, O, N, and C atoms close to Er were described by ANO-RCC-VDZP basis sets [167]. Further distant C and H atoms were described by the same basis but without polarization. Spin-orbit interaction was considered within RASSI code and included 35 spin quartet states, optimized within a state-average CASSCF calculation. Dynamic correlation was considered within the CASPT2 method and made use of the recently implemented extended multistate feature [116,117]. The application of the conventional multistate CASPT2 method is compromised by its inability to preserve exact degeneracies. As a matter of fact, for free lanthanide ions, the spurious splitting of exactly degenerate

states of the atomic J multiplet predicted within the standard multistate CASPT2 method is of the same order of magnitude as the crystal-field splitting arising due to ligands' environment. This makes the conventional CASPT2 approach rather inapplicable for the calculation of the low-lying part of the crystal-field splitting in lanthanides. Standard multistate NEVPT2 may suffer from similar issues. In contrast, the extended MS-CASPT2 version (also available in MOLPRO package) does not suffer from this problem. In all CASPT2 calculations, the IPEA shift [168] was set to 0.0 Ha (in place of the default 0.25 Ha), and the imaginary shift was set to 0.1 Ha to avoid intruder state problems. The code's default choice for the number of frozen orbitals was kept unaltered. The electrostatic effect of the crystal environment (Madelung potential) was modeled as follows: each atom from the neighboring five layers of unit cells of molecules was modeled by its own Mulliken charge obtained in the previous calculation.

Table 1.5 shows the results of the *ab initio* calculations with a varying level of accuracy in comparison with the spectrum of crystal-field multiplets extracted from measurements of luminescence. The models A1 and A3 in Table 1.5 show a close agreement with previously reported *ab initio* results on this compound [164], albeit employing a larger basis set. The Madelung electrostatic field of the crystal has a similar effect in all computational models: it reduces the energies of Kramers doublets 2, 3, 4, 6, 7, and 8 by ca. 5–10 cm^{-1}, and it increases the energy of the Kramers doublet 5 by ca. 2–5 cm^{-1}. A more noticeable effect of the Madelung potential is seen on the g tensor of the ground Kramers doublet: g_X and g_Y values increased, while g_Z is reduced.

Table 1.5 Low-lying energy spectrum (in cm^{-1}) and g factors of the ground Kramers doublet of Er-trensal obtained by CASSCF/CASPT2/RASSI computation

CASPT2 Effect from neighbor molecules[a]	Not included Not included	Included Not included	Not included Included	Included Included
Model	**A1**	**A2**	**A3**	**A4**	**Exp. [164–166][a]**
CASSCF active space: CAS(11 in 7) ($4f^{11}$ shell)					
1	0.0	0.0	0.0	0.0	0
2	61.4	83.4	53.4	75.7	54
3	100.9	140.3	92.2	129.4	102
4	101.3	149.1	97.0	145.0	110
5	211.2	359.4	213.3	362.7	299
6	413.1	607.1	404.6	597.8	568
7	454.8	677.0	447.1	668.8	610
8	482.9	724.1	473.9	713.2	642
g_X	2.33	3.13	2.80	3.82	3.36
g_Y	2.33	3.17	2.80	3.87	3.36
g_Z	13.69	12.60	13.05	11.58	11.90

Table 1.5 Continued

Model	B1	B2	B3	B4	Exp. [164–166][a]
CASSCF active space: CAS(11 in 14) ($4f^{11}$+$5f^{0}$ shell)					
1	0.0	0.0	0.0	0.0	0
2	69.7	80.5	60.5	71.7	54
3	109.4	130.0	99.6	119.4	102
4	110.1	132.2	104.1	127.6	110
5	239.4	304.4	239.8	308.6	299
6	441.5	547.8	431.4	538.7	568
7	486.2	599.2	476.9	591.4	610
8	517.9	635.4	506.7	625.6	642
g_X	2.47	2.74	3.00	3.33	3.36
g_Y	2.47	2.75	3.00	3.35	3.36
g_Z	13.55	13.16	12.82	12.32	11.90
Model	**C1**	**C2**	**C3**	**C4**	**Exp. [164–166][a]**
RASSCF active space: CAS(17 in 25) (Ras1, $5p^{6}$; Ras2, $4f^{11}$, Ras3, $5f^{0}$, $5d^{0}$, and $6p^{0}$)[b]					
1	0.0	0.0	0.0	0.0	0
2	61.9	71.6	52.7	63.3	54
3	105.2	121.1	94.8	110.9	102
4	107.4	125.4	102.2	121.0	110
5	233.4	293.2	234.4	297.6	299
6	453.7	534.2	443.9	525.2	568
7	499.1	582.4	490.1	574.6	610
8	528.8	613.3	518.0	603.9	642
g_X	2.50	2.77	3.08	3.42	3.36
g_Y	2.50	2.78	3.09	3.45	3.36
g_Z	13.49	13.08	12.68	12.14	11.90

[a]Electrostatic effect of the crystal (Madelung potential) was modeled by Mulliken atomic charges of five layers of surrounding unit cells of molecules.
[b]Configurations with maximum two holes in Ras1 and maximum two electrons in Ras3 were allowed.

Despite the relative good agreement for the lowest three excitation energies of the A3 model, the total splitting (473 cm^{-1}) is clearly underestimated compared with the measured one (642 cm^{-1}). We notice that in all cases (models 2 and 4, all active spaces), the effect of dynamic correlation leads to an increase of the total splitting of the ground atomic $J = 15/2$ of Er^{3+} compared with the corresponding CASSCF/RASSI results. In the case of minimal active space (models A2 and A4), the increase of the crystal-field splitting is larger than the measured one, an effect attenuated by larger active spaces. The increase of the total splitting has as a drawback the poorer description of the low-lying excited states. A similar trend is noticed for the transversal g factors of the ground Kramers doublet, $g_{X,Y}$, which become larger than their

uncorrelated equivalents, while the effect of the Madelung potential makes $g_{X,Y}$ even larger than the experimental ones (Table 1.5).

The increase in the active space by the addition of the double shell—another set of seven metal-based f orbitals—leads to a significant improvement in the results (models B2 and B4). In these cases, the total splitting of the ground $J = 15/2$ multiplet is in almost perfect agreement with the total splitting obtained experimentally. Even more, a correct trend for the excitation energies of all Kramers doublets is noticed. Calculated g tensors of the ground Kramers doublets are also in an almost ideal agreement with experimental data. Since by increasing the active space we actually include some of the dynamic correlation at the CASSCF level, the "overshooting" effect of the CASPT2 is not seen anymore, which is a nice point of this approach. The same is true for the ground-state g tensor (Fig. 1.9).

Finally, the active space was further increased by including $5p^6$, $5d^0$, $6p^0$, and $5f^0$ orbital configurations in addition to the minimal active space. Since the number of configurations generated within the CASSCF method becomes very large for such an extended active space, we employed the RAS restrictions (see Table 1.5). RASPT2 calculations [101,108,169,170] were performed on top of the optimized RASSCF wave functions. Since more of the dynamic correlation is accounted for at RASSCF level, we notice an increase of the total splitting for models C1 and C3 (uncorrelated)

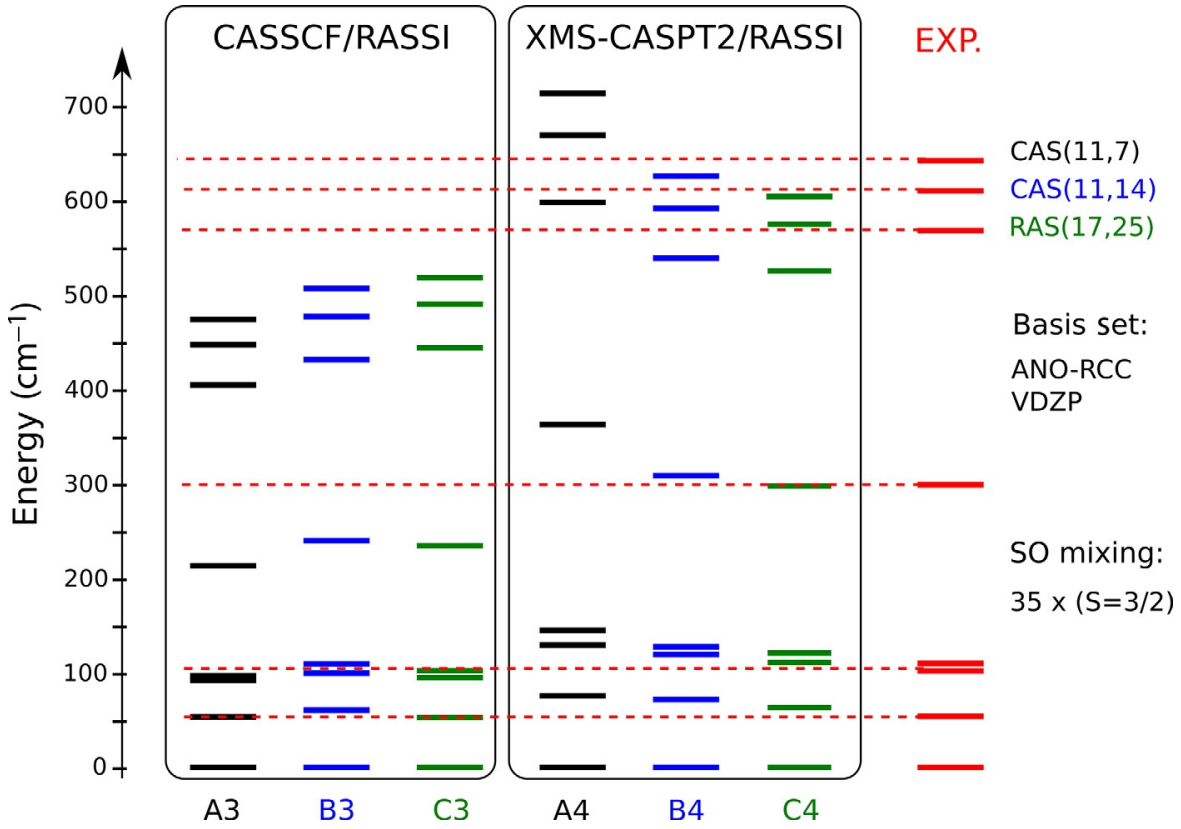

Fig. 1.9 A comparison between various *ab initio* approaches to the calculation of crystal-field spectrum of Er-trensal with data extracted from luminescence [166]. All *ab initio* calculations included the Madelung potential. Labels stand for specific computational models listed in Table 1.5.

compared with smaller active spaces A1, A3, B1, and B3, respectively, corroborated by an increase in the $g_{X,Y}$ values for the ground Kramers doublet. This is clearly an effect of additional dynamic correlation included at the RASSCF level. As a result, there is less correlation to be included at the RASPT2 level of theory. Consequently, the differences between the C and B models are smaller compared with A models, respectively. One also finds that dynamic correlation also contributes to a better description of the static magnetic properties: magnetic susceptibility and molar magnetization [57].

One may conclude that the dynamic correlation effects for lanthanide compounds is a necessary ingredient for accurate estimation of crystal-field spectrum and magnetic/electronic properties of individual crystal-field doublets of lanthanide complexes, provided that the active space of the CASSCF method is chosen large enough (like in models B or C) to counteract the overshooting effect of the second-order perturbation theory seen for the minimal active spaces. Given the small energy differences in the crystal-field levels of lanthanides, the weak electrostatic effect of the crystal (the Madelung potential) also plays an important role to improve the overall accuracy.

Dynamic electron correlation was considered in other studies related to lanthanides [84,171,172].

1.3.7 *Semi*-ab initio *description of electronic and magnetic structures of polynuclear compounds*

The description of the electronic structure and magnetism of polynuclear compounds is extremely challenging for current *ab initio* methods. The difficulties arise due to several factors: firstly, because of the larger dimension of the active space of the CASSCF method required, which must include all frontier molecular orbitals (e.g., all sets of 3*d* and 4*f* shells containing unpaired electrons); secondly, due to the much larger number of spin states required to be included in the spin-orbit coupling for the polynuclear compound; and, thirdly, because of the requisites for the numerical accuracy of the calculation, which are much tighter for the dynamic correlation methods (e.g., CASPT2) and which, ideally, would need to provide accurate energy differences within $<1\,\mathrm{cm}^{-1}$ (and, if possible, lower). For obvious reasons, such computational and numerical difficulties preclude, at least for now, the direct application of existing *ab initio* methods to polynuclear lanthanide-based systems.

Density functional theory calculations of the magnetic exchange coupling parameter (i.e., broken-symmetry DFT [173]) have been done for Gd-transition-metal (TM) and Gd-radical (R) complexes, but cannot be directly applied to other lanthanide ions due to the near-degeneracy and multiconfigurational nature of the ground- and low-lying excited-state wave functions, which precludes the application of DFT, in principle. Luckily, given the strong magnetic axiality displayed by lanthanide ions, the magnetic exchange between two lanthanide ions (Ln1-Ln2) or the interactions between a lanthanide ion and an isotropic spin or a radical (Ln-S) reduce to the Ising-type interaction between the lowest double states. The latter can be accurately described within a semiempirical two-step approach reviewed in this section.

To overcome these computational difficulties, a semi-*ab initio* approach was developed that allows to describe with reasonable accuracy the low-lying electronic and magnetic structures for polynuclear compounds [22,126,127]. The method is based on several steps:

- **(i)** Breaking down of the polynuclear compound into several mononuclear fragments, such that the localized electronic structure of each metal site is not significantly affected. This involves the computational substitution of all neighboring metal sites of a given center for their diamagnetic equivalents (e.g., neighboring effect of the Dy^{3+} is computationally modeled with reasonable accuracy by the diamagnetic (closed shell) Lu^{3+} ion), while the ligand framework is left unaltered in all fragments.
- **(ii)** Computational investigation of each fragment by *ab initio* means (e.g., CASSCF/CASPT2/RASSI/SINGLE_ANISO). Localized spin-orbit energy structure, local spin moment, and magnetic moment local magnetic properties (g and D tensors, magnetic susceptibility, and molar magnetization) are obtained for each fragment/metal site.
- **(iii)** The total interaction Hamiltonian (magnetic exchange + magnetic dipole-dipole interaction) is built and diagonalized in the basis of the products of the local *ab initio* wave functions and eigenstates obtained for the individual metal sites at (ii). The magnetic exchange interactions between metal fragments are included in an effective (phenomenological) way using the line approximation [174]. Magnetic dipole-dipole interaction between different centers is computed exactly, since all local magnetic properties are known.
- **(iv)** Computation of magnetic properties of the entire polynuclear compound using the obtained exchange eigenstates at (iii), also accounting for the magnetic moment of the local states that were not included in the exchange basis.
- **(v)** Extraction of the strength of the magnetic interaction from the direct comparisons between computed and measured magnetic data.

The above described algorithm was proposed, implemented, and employed for the first time for the investigation of the origin of nonmagnetic ground state of a Dy_3 triangle [126,127]. The algorithm was implemented in the POLY_ANISO software and is available as a module in MOLCAS package [101] and also as a stand-alone program.

Figs. 1.10 and 1.11 show the local energy structure of individual Dy sites in Dy_3 triangle. The obtained local main magnetic axis (g_Z) lies in the plane of the Dy_3 molecule, making an angle of ca. 60 degree with each other. The magnetic moments of each center approach their limit with values of $g_Z \approx 20\ \mu_B$. The magnetic moments of each center along the other two local axes ($g_{X,Y}$) are very small ($<0.1\ \mu_B$), which means that the magnetization of the individual Dy site can only occur along its own g_Z axis. Given the fact that magnetic exchange is rather weak and that it occurs only between low-lying energy states, it leads to certain correlated arrangements of the local moments. In this Dy_3 triangle, the dipole-dipole interaction alone leads to the stabilization of the toroidal (nonmagnetic) arrangement in the ground state. Exchange interaction between sites further contributed to this stabilization. Magnetic excited exchange states (three Kramers doublets, where one moment is reversed w.r.t. the Fig. 1.10B) are around $7.5\,cm^{-1}$ higher than the ground nonmagnetic state. At low temperatures, Boltzmann population of excited states is rather small; therefore, only the total moment of the ground state (which is very close to zero, i.e., nonmagnetic) is detected.

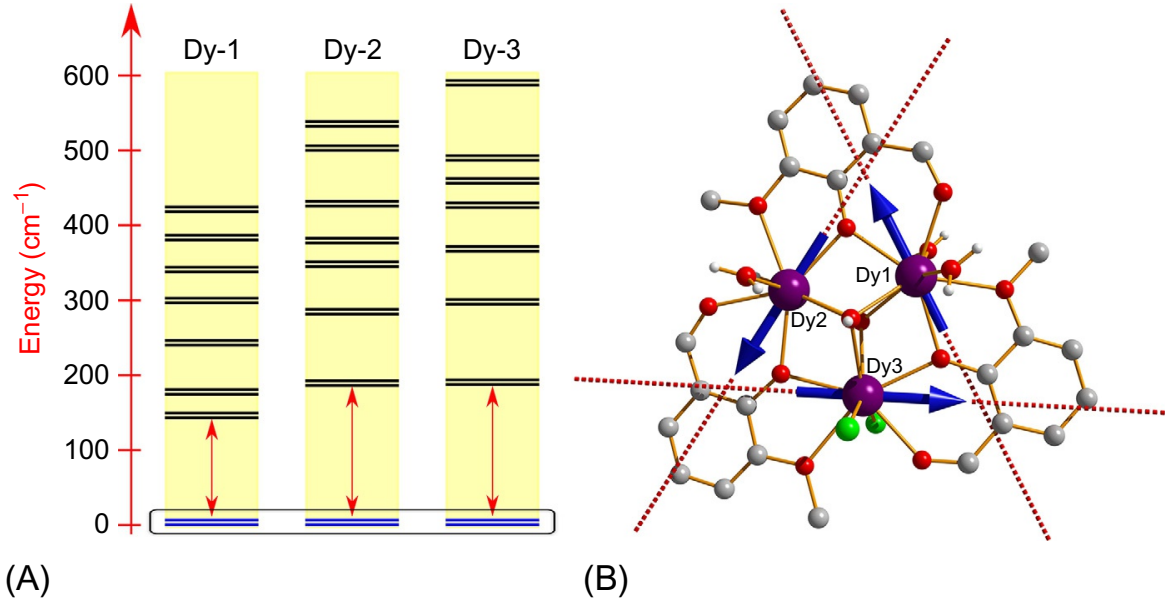

Fig. 1.10 (A) Energy structure of the ground $J = 15/2$ multiplet of the Dy^{3+} sites in the Dy_3 triangle [175]. (B) Molecular structure of the Dy_3 triangle. *Dashed lines* represent the main magnetic axis (g_Z) of the ground Kramers doublet of each site ($g_{X,Y} \sim 0$ and $g_Z \sim 20\ \mu_B$ for each Dy site). *Blue arrows* represent the arrangement of local moments in one of the two components of the ground exchange state of the entire Dy_3 triangle. The toroidal arrangement of local moments is the reason why the molecule is not magnetic at low temperature.

Resulting molar magnetization is rather small. Since magnetic excited states strongly interact with the applied magnetic field, they become ground states already at fields of ca. 0.9 T. This is the reason for the sharp jump in the molar magnetization at 1.8 K (Fig. 1.11A). Overall, this computational methodology allows a surprisingly good description of the measured magnetic properties for this compound (Fig. 1.11). In particular, experimental extracted orientation of the local axes shows agreement with theoretical predicted axes within a few degrees [176,177].

The class of compounds with toroidal magnetization in the ground state are called single-molecule toroics (SMT) [178–181] and have attracted significant attention due to their possible usage as quantum information units, since toroidal moment may be controlled by an electric field [182,183]. The noncollinear magnetic structure lies at the core of a large number of interesting phenomena such as spin glass [184] and multiferroic behavior [185–187].

Since then, this methodology has been applied to/validated on a wide variety of polynuclear compounds containing lanthanides and/or transition metals as core magnetic ingredients [188–192].

1.4 Conclusions and outlook

Theoretical/computational description of the electronic structure and properties of materials containing lanthanide ions has a history of several decades. Since the early

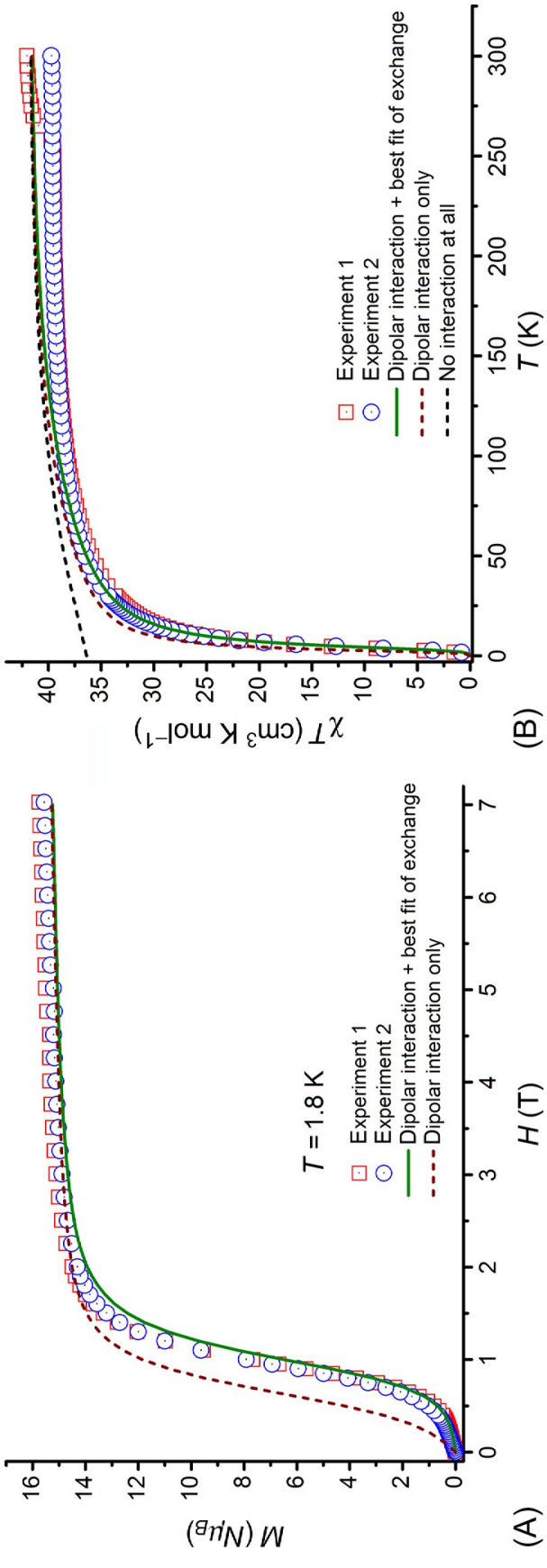

Fig. 1.11 Semi-*ab initio* description of the (A) powder molar magnetization and (B) powder molar magnetic susceptibility for the Dy_3 triangle. The effect of magnetic exchange and dipole-dipole interactions on computed magnetic properties is displayed as well.

days, this task has been very challenging due to many factors, many of them deriving from the peculiarity of the *relatively weak* but *important* interaction between the 4*f* shell with other metals' and ligands' orbitals.

A review of electronic and magnetic structure of free lanthanide ions has been given, alongside a brief discussion of the main phenomenological models used for the rationalization of experimental optical and magnetic data.

We have shown here that the *ab initio* calculations based on CASSCF/CASPT2/RASSI/SINGLE_ANISO implemented in MOLCAS package provide a description of magnetic properties with experimental accuracy, while the parameters of pseudospin magnetic Hamiltonians describing these properties can be routinely derived from the results of these calculations. They have been valuable for the field of molecular magnetism, allowing the rationalization and prediction of the magnetization blocking behavior of various existing and model compounds. The importance of the dynamic electronic correlation for accurate predictions of the electronic structure and the properties of lanthanide-based compounds has been demonstrated. The *ab initio* methodology, complemented by a phenomenological description of anisotropic exchange interactions within the Lines model, has proved successful for the description of a large variety of polynuclear compounds involving lanthanides.

With respect to optical properties, *ab initio* methods are still less frequently applied than the phenomenological Judd-Ofelt approach. Among many reasons, the description of optical processes is still a heavy computational task, which required the treatment of large active spaces and an accurate account of a (very) large amount of states originating from the ground and excited configurations. Important progress in the field of electronic structure methods, which already led to the development of DMRG and FCIQMC methods that allow optimizations of large active spaces, and the novel electron correlation methods that allow the accurate description of ground and excited states for multireference wave functions gives confidence that the *ab initio* methodology will allow for quantitative description of optical properties of lanthanide compounds.

As future work regarding magnetic properties of lanthanide-based materials, there is clearly a need to describe magnetic relaxation processes of molecular magnets at the *ab initio* level and the intricate nature of the intra- and intermolecular magnetic (exchange) interactions. Some promising research in this direction gives grounded hopes that this task is realistic, for example, [193–195].

Given the multitude of existing and novel computational methods, future work is needed to benchmark their performance for the description of near-degenerate ground and excited states, without inducing unphysical (erroneous) splittings. Work is also required to test various methods accounting for the environment effects (embedding) and to assess the errors induced by various integral approximations (such as resolution of identity, Cholesky decomposition of molecular integrals [196,197], or density-fitting-based methods [198,199]) for the dense, near-degenerate energy spectra of lanthanide systems. Recently, efforts are being made to develop *ab initio* methods with reduced scaling compared with CASSCF/RASSI approach [200–202].

References

[1] K. Binnemans, Lanthanide-based luminescent hybrid materials, Chem. Rev. 109 (2009) 4283–4374, https://doi.org/10.1021/cr8003983.

[2] M. Bottrill, L. Kwok, N.J. Long, Lanthanides in magnetic resonance imaging, Chem. Soc. Rev. 35 (2006) 557, https://doi.org/10.1039/b516376p.

[3] J.C.G. Bünzli, S.V. Eliseeva, Lanthanide NIR luminescence for telecommunications, bioanalyses and solar energy conversion, J. Rare Earths 28 (2010) 824–842, https://doi.org/10.1016/S1002-0721(09)60208-8.

[4] J.C.G. Bünzli, S. Comby, A.S. Chauvin, C.D.B. Vandevyver, New opportunities for lanthanide luminescence, J. Rare Earths 25 (2007) 257–274, https://doi.org/10.1016/S1002-0721(07)60420-7.

[5] J. Schoenes, Magneto-optic lanthanide materials, J. Alloys Compd. 250 (1997) 627–634, https://doi.org/10.1016/S0925-8388(96)03036-8.

[6] R. Reisfeld, Optical properties of lanthanides in condensed phase, theory and applications, AIMS Mater. Sci. 2 (2015) 37–60, https://doi.org/10.3934/matersci.2015.2.37.

[7] J. Rocha, L.D. Carlos, F.A.A. Paz, D. Ananias, Luminescent multifunctional lanthanides-based metal-organic frameworks, Chem. Soc. Rev. 40 (2011) 926–940, https://doi.org/10.1039/C0CS00130A.

[8] F. Wang, X. Liu, Recent advances in the chemistry of lanthanide-doped upconversion nanocrystals, Chem. Soc. Rev. 38 (2009) 976–989, https://doi.org/10.1039/b809132n.

[9] J.C.G. Bünzli, Lanthanide luminescence: from a mystery to rationalization, understanding, and applications, Handb. Phys. Chem. Rare Earths (2016) 141–176, https://doi.org/10.1016/bs.hpcre.2016.08.003.

[10] N. Ishikawa, Single molecule magnet with single lanthanide ion, Polyhedron 26 (2007) 2147–2153, https://doi.org/10.1016/j.poly.2006.10.022.

[11] D.N. Woodruff, R.E. Winpenny, R.A. Layfield, Lanthanide single-molecule magnets, Chem. Rev. (2013), https://doi.org/10.1021/cr400018q.

[12] R. Sessoli, K. Bernot, Lanthanides in extended molecular networks, in: Lanthanides Actinides Molecular Magnetism, 2015, pp. 89–124, https://doi.org/10.1002/9783527673476.ch4.

[13] J. Luzon, R. Sessoli, Lanthanides in molecular magnetism: so fascinating, so challenging, Dalton Trans. 41 (2012) 13556, https://doi.org/10.1039/c2dt31388j.

[14] R. Sessoli, A.K. Powell, Strategies towards single molecule magnets based on lanthanide ions, Coord. Chem. Rev. (2009), https://doi.org/10.1016/j.ccr.2008.12.014.

[15] F.D. Natterer, K. Yang, W. Paul, P. Willke, T. Choi, T. Greber, A.J. Heinrich, C.P. Lutz, Reading and writing single-atom magnets, Nature 543 (2017) 226–228, https://doi.org/10.1038/nature21371.

[16] S. Freer, S. Simmons, A. Laucht, J.T. Muhonen, J.P. Dehollain, R. Kalra, F. A. Mohiyaddin, F.E. Hudson, K.M. Itoh, J.C. McCallum, D.N. Jamieson, A.S. Dzurak, A. Morello, A single-atom quantum memory in silicon, Quantum Sci. Technol. 2 (2017) 15009, https://doi.org/10.1088/2058-9565/aa63a4.

[17] B.T. Kilbourn, The role of the lanthanides in applied catalysis, J. Less-Common Met. 126 (1986) 101–106, https://doi.org/10.1016/0022-5088(86)90254-7.

[18] M. Shibasaki, N. Yoshikawa, Lanthanide complexes in multifunctional asymmetric catalysis, Chem. Rev. 102 (2002) 2187–2209, https://doi.org/10.1021/cr010297z.

[19] N.R. Natale, Lanthanides in organic synthesis, Org. Prep. Proced. Int. 15 (1983) 387–424, https://doi.org/10.1080/00304948309355449.

[20] P.A. Tanner, Lanthanide luminescence in solids, in: Lanthanide Luminescence, 2010, , pp. 183–233, https://doi.org/10.1007/4243_2010_6.
[21] D. Gatteschi, R. Sessoli, J. Villain, Molecular Nanomagnets, (2007), https://doi.org/10.1093/acprof:oso/9780198567530.001.0001.
[22] L. Ungur, L.F. Chibotaru, Computational modelling of the magnetic properties of lanthanide compounds, in: Lanthanides and Actinides in Molecular Magnetism, 2015, https://doi.org/10.1002/9783527673476.ch6.
[23] R.A. Layfield, M. Murugesu, Lanthanides and Actinides in Molecular Magnetism, 2015. https://doi.org/10.1002/9783527673476.
[24] D. Goll, H. Kronmüller, High-performance permanent magnets, Naturwissenschaften 87 (2000) 423–438, https://doi.org/10.1007/s001140050755.
[25] J.F. Herbst, J.J. Croat, Neodymium-iron-boron permanent magnets, J. Magn. Magn. Mater. 100 (1991) 57–78, https://doi.org/10.1016/0304-8853(91)90812-O.
[26] N. Poudyal, J. Ping Liu, Advances in nanostructured permanent magnets research, J. Phys. D: Appl. Phys. 46 (2013), https://doi.org/10.1088/0022-3727/46/4/043001.
[27] S.V. Eliseeva, J.-C.G. Bünzli, Lanthanide luminescence for functional materials and bio-sciences, Chem. Soc. Rev. 39 (2010) 189–227, https://doi.org/10.1039/B905604C.
[28] A.J. Amoroso, S.J.A. Pope, Using lanthanide ions in molecular bioimaging, Chem. Soc. Rev. 44 (2015) 4723–4742, https://doi.org/10.1039/C4CS00293H.
[29] O. Svelto, Principles of Lasers, Springer, 2010, https://doi.org/10.1007/978-1-4419-1302-9.
[30] K. Wendt, T. Gottwald, C. Mattolat, S. Raeder, Ionization potentials of the lanthanides and actinides—towards atomic spectroscopy of super-heavy elements, Hyperfine Interact. 227 (2014) 55–67, https://doi.org/10.1007/s10751-014-1041-8.
[31] W.C. Martin, L. Hagan, J. Reader, J. Sugar, Ground levels and ionization potentials for lanthanide and actinide atoms and ions, J. Phys. Chem. Ref. Data 3 (1974) 771–780, https://doi.org/10.1063/1.3253147.
[32] M. Dolg, P. Fulde, H. Stoll, H. Preuss, A. Chang, R.M. Pitzer, Formally tetravalent cerium and thorium compounds: a configuration interaction study of cerocene $Ce(C_8H_8)_2$ and thorocene $Th(C_8H_8)_2$ using energy-adjusted quasirelativistic ab initio pseudopotentials, Chem. Phys. 195 (1995) 71–82, https://doi.org/10.1016/0301-0104(94)00363-F.
[33] F. Nief, Molecular chemistry of the rare-earth elements in uncommon low-valent states, Handb. Phys. Chem. Rare Earths 40 (2010) 241–300, https://doi.org/10.1016/S0168-1273(10)40006-9 (Chapter 246).
[34] M.R. Macdonald, J.E. Bates, J.W. Ziller, F. Furche, W.J. Evans, Completing the series of +2 ions for the lanthanide elements: synthesis of molecular complexes of Pr^{2+}, Gd^{2+}, Tb^{2+}, and Lu^{2+}, J. Am. Chem. Soc. 135 (2013) 9857–9868, https://doi.org/10.1021/ja403753j.
[35] W.C. Martin, R. Zalubas, L. Hagan, Atomic Energy Levels: The Rare-Earth Elements (the Spectra of Lanthanum, Cerium, Praseodymium, Neodymium, Promethium, Samarium, Europium, Gadolinium, Terbium, Dysprosium, Holmium, Ebrium, Thulium, Ytterbium, and Lutetium), (1978), https://doi.org/10.6028/NBS.NSRDS.60.
[36] D.A. Varshalovich, A.N. Moskalev, V.K. Khersonskii, Quantum Theory of Angular Momentum, World Scientific, 1988, https://doi.org/10.1142/0270.
[37] K.G. Dyall, K. Fægri, Introduction to Relativistic Quantum Chemistry, Oxford University Press, 2007. https://global.oup.com/academic/product/introduction-to-relativistic-quantum-chemistry-9780195140866?cc=be&lang=en&. Accessed 20 December 2017.

[38] M. Reiher, A. Wolf, Relativistic Quantum Chemistry: The Fundamental Theory of Molecular Science, second ed., Wiley-VCH, 2015, https://doi.org/10.1002/9783527667550.
[39] A.K. Zvezdin, V.M. Matveev, A.A. Mukhin, A.I. Popov, Rare earth ions in magnetically ordered crystals, Moscow, Izd. Nauk. 1985 (1985) 296 (in Russian).
[40] A. Abragam, B. Bleaney, Electron Paramagnetic Resonance of Transition Ions, Oxford University Press, 1970, https://doi.org/10.1017/CBO9781107415324.004.
[41] J. Mulak, Z. Gajek, The Effective Crystal Field Potential, Elsevier, 2000, https://doi.org/10.1016/B978-008043608-1/50005-8.
[42] C. Görller-Walrand, K. Binnemans, Rationalization of crystal-field parametrization, Handb. Phys. Chem. Rare Earths 23 (1996) 121–283, https://doi.org/10.1016/S0168-1273(96)23006-5 (Chapter 155).
[43] B.G. Wybourne, Spectroscopic Properties of Rare Earths, John Wiley, New York, 1965.
[44] H. Bethe, Termaufspaltung in Kristallen, Ann. Phys. 395 (1929) 133–208, https://doi.org/10.1002/andp.19293950202.
[45] J.H. Van Vleck, The puzzle of rare-earth spectra in solids, J. Phys. Chem. 41 (1937) 67–80, https://doi.org/10.1021/j150379a006.
[46] A. Abragam, M.H.L. Pryce, The theory of paramagnetic resonance in hydrated cobalt salts, Proc. R. Soc. A Math. Phys. Eng. Sci. 206 (1951) 173–191, https://doi.org/10.1098/rspa.1951.0063.
[47] J.J. Baldoví, J.J. Borrás-Almenar, J.M. Clemente-Juan, E. Coronado, A. Gaita-Ariño, Modeling the properties of lanthanoid single-ion magnets using an effective point-charge approach, Dalton Trans. 41 (2012) 13705, https://doi.org/10.1039/c2dt31411h.
[48] R.R. Sharma, Expansion of a function about a displaced center for multicenter integrals: a general and closed expression for the coefficients in the expansion of a Slater orbital and for overlap integrals, Phys. Rev. A 13 (1976) 517–527, https://doi.org/10.1103/PhysRevA.13.517.
[49] H.S. Jarrett, Generalization of crystal field theory to include covalent bonding, J. Chem. Phys. 31 (1959) 1579–1585, https://doi.org/10.1063/1.1730655.
[50] C.E. Schäffer, A perturbation representation of weak covalent bonding, in: Structure and Bonding, Springer Berlin Heidelberg, Berlin, Heidelberg, 1968, , pp. 68–95, https://doi.org/10.1007/BFb0118847.
[51] C.K. Jo/rgensen, R. Pappalardo, H. Schmidtke, Do the "ligand field" parameters in lanthanides represent weak covalent bonding? J. Chem. Phys. 39 (1963) 1422–1430, https://doi.org/10.1063/1.1734458.
[52] J.J. Baldoví, S. Cardona-Serra, J.M. Clemente-Juan, E. Coronado, A. Gaita-Ariño, A. Palii, SIMPRE: a software package to calculate crystal field parameters, energy levels, and magnetic properties on mononuclear lanthanoid complexes based on charge distributions, J. Comput. Chem. 34 (2013) 1961–1967, https://doi.org/10.1002/jcc.23341.
[53] M. Karbowiak, C. Rudowicz, Software package SIMPRE—revisited, J. Comput. Chem. 35 (2014) 1935–1941, https://doi.org/10.1002/jcc.23700.
[54] N.F. Chilton, R.P. Anderson, L.D. Turner, A. Soncini, K.S. Murray, PHI: a powerful new program for the analysis of anisotropic monomeric and exchange-coupled polynuclear *d* - and *f*-block complexes, J. Comput. Chem. 34 (2013) 1164–1175, https://doi.org/10.1002/jcc.23234.
[55] M. Speldrich, H. Schilder, H. Lueken, P. Kögerler, A computational framework for magnetic polyoxometalates and molecular spin structures: CONDON 2.0, Isr. J. Chem. 51 (2011) 215–227, https://doi.org/10.1002/ijch.201100013.

[56] L.F. Chibotaru, L. Ungur, Ab initio calculation of anisotropic magnetic properties of complexes. I. Unique definition of pseudospin Hamiltonians and their derivation, J. Chem. Phys. 137 (2012), https://doi.org/10.1063/1.4739763.
[57] L. Ungur, L.F. Chibotaru, Ab initio crystal field for lanthanides, Chem. Eur. J. 23 (15) (2017) 3708–3718, https://doi.org/10.1002/chem.201605102.
[58] S.K. Singh, J. Eng, M. Atanasov, F. Neese, Covalency and chemical bonding in transition metal complexes: an ab initio based ligand field perspective, Coord. Chem. Rev. 344 (2017) 2–25, https://doi.org/10.1016/j.ccr.2017.03.018.
[59] J. Jung, M. Atanasov, F. Neese, Ab initio ligand-field theory analysis and covalency trends in actinide and lanthanide free ions and octahedral complexes, Inorg. Chem. 56 (2017) 8802–8816, https://doi.org/10.1021/acs.inorgchem.7b00642.
[60] B.R. Judd, Optical absorption intensities of rare-earth ions, Phys. Rev. 127 (1962) 750–761, https://doi.org/10.1103/PhysRev.127.750.
[61] G.S. Ofelt, Intensities of crystal spectra of rare-earth ions, J. Chem. Phys. 37 (1962) 511–520, https://doi.org/10.1063/1.1701366.
[62] C. Eckart, The application of group theory to the quantum dynamics of monatomic systems, Rev. Mod. Phys. 2 (1930) 305–380, https://doi.org/10.1103/RevModPhys.2.305.
[63] E. Wigner, Einige folgerungen aus der schrödingerschen theorie für die termstrukturen, Z. Phys. 43 (1927) 624–652, https://doi.org/10.1007/BF01397327.
[64] B.M. Walsh, Judd-Ofelt theory: principles and practices, in: Adv. Spectrosc. Lasers Sens., Springer Netherlands, Dordrecht, 2006, pp. 403–433, https://doi.org/10.1007/1-4020-4789-4_21.
[65] C.W. Nielson, Spectroscopic Coefficients for the pn, dn, and fn Configurations, M.I.T. Press, Cambridge, MA, 1963. *http://hdl.handle.net/2027/mdp.39015078650028*. Accessed 19 December 2017.
[66] E.P. Wigner, J.J. Griffin, Group Theory and its Application to the Quantum Mechanics of Atomic Spectra, Academic Press, Cambridge, 1959.
[67] B.G. Wybourne, L. Smentek, Relativistic effects in lanthanides and actinides, J. Alloys Compd. (2002) 71–75, https://doi.org/10.1016/S0925-8388(02)00066-X.
[68] L. Smentek, B.G. Wybourne, Relativistic f ↔ f transitions in crystal fields: II. Beyond the single-configuration approximation, J. Phys. B: At. Mol. Opt. Phys. 34 (2001) 625–630, https://doi.org/10.1088/0953-4075/34/4/310.
[69] L. Smentek, B.G. Wybourne, J. Kobus, A relativistic crystal field for S-state f electron ions, J. Phys. B: At. Mol. Opt. Phys. 34 (2001) 1513–1522, https://doi.org/10.1088/0953-4075/34/8/314.
[70] L. Smentek, B.G. Wybourne, B.A. Hess Jr., Judd–Ofelt theory in a new light on its (almost) 40th anniversary, J. Alloys Compd. 323–324 (2001) 645–648, https://doi.org/10.1016/S0925-8388(01)01185-9.
[71] J.C. Slater, The theory of complex spectra, Phys. Rev. 34 (1929) 1293–1322, https://doi.org/10.1103/PhysRev.34.1293.
[72] G. Racah, Theory of complex spectra. I, Phys. Rev. 61 (1942) 186–197, https://doi.org/10.1103/PhysRev.61.186.
[73] G. Racah, Theory of complex spectra. II, Phys. Rev. 62 (1942) 438–462, https://doi.org/10.1103/PhysRev.62.438.
[74] G. Racah, Theory of complex spectra. III, Phys. Rev. 63 (1943) 367–382, https://doi.org/10.1103/PhysRev.63.367.
[75] G. Racah, Theory of complex spectra. IV, Phys. Rev. 76 (1949) 1352–1365, https://doi.org/10.1103/PhysRev.76.1352.

[76] E.U. Condon, The theory of complex spectra, Phys. Rev. 36 (1930) 1121–1133, https://doi.org/10.1103/PhysRev.36.1121.
[77] X. Shangda, C. Yimin, Effect of J-mixing on the intensities of f-f transitions of rare earth ions, J. Lumin. 31–32 (1984) 204–206, https://doi.org/10.1016/0022-2313(84)90248-5.
[78] M. Tanaka, G. Nishimura, T. Kushida, Contribution of J mixing to the $^5D_0$-$^7F_0$ transition of Eu^{3+} ions in several host matrices, Phys. Rev. B 49 (1994) 16917–16925, https://doi.org/10.1103/PhysRevB.49.16917.
[79] M. Tanaka, T. Kushida, J-mixing effect on the vibronic spectra of Eu^{3+} ions, J. Alloys Compd. 193 (1993) 183–185, https://doi.org/10.1016/0925-8388(93)90343-L.
[80] L. Smentek, B.A. Hess, Theoretical description of $0 \leftrightarrow 0$ and $0 \leftrightarrow 1$ transitions in the Eu^{3+} ion in hosts with C_{2v} symmetry, Mol. Phys. 92 (1997) 835–846, https://doi.org/10.1080/002689797169781.
[81] E.B. Dunina, A.A. Kornienko, L.A. Fomicheva, Modified theory of *f-f* transition intensities and crystal field for systems with anomalously strong configuration interaction, Centr. Eur. J.Phys. 6 (2008) 407–414, https://doi.org/10.2478/s11534-008-0084-3.
[82] L. Smentek, Effective operators and spectroscopic properties, J. Alloys Compd. 380 (2004) 89–95, https://doi.org/10.1016/j.jallcom.2004.03.033.
[83] J. Wen, M.F. Reid, L. Ning, J. Zhang, Y. Zhang, C.K. Duan, M. Yin, Ab-initio calculations of Judd-Ofelt intensity parameters for transitions between crystal-field levels, J. Lumin. 152 (2014) 54–57, https://doi.org/10.1016/j.jlumin.2013.10.055.
[84] M. Dolg, Computational Methods in Lanthanide and Actinide Chemistry, (2015), https://doi.org/10.1002/9781118688304.
[85] N. Ishikawa, M. Sugita, T. Ishikawa, S.Y. Koshihara, Y. Kaizu, Lanthanide double-decker complexes functioning as magnets at the single-molecular level, J. Am. Chem. Soc. 125 (2003) 8694–8695, https://doi.org/10.1021/ja029629n.
[86] N. Ishikawa, M. Sugita, T. Ishikawa, S.Y. Koshihara, Y. Kaizu, Mononuclear lanthanide complexes with a long magnetization relaxation time at high temperatures: a new category of magnets at the single-molecular level, J. Phys. Chem. B 108 (2004) 11265–11271, https://doi.org/10.1021/jp0376065.
[87] R. Sessoli, D. Gatteschi, A. Caneschi, M.A. Novak, Magnetic bistability in a metal-ion cluster, Nature 365 (1993) 141–143, https://doi.org/10.1038/365141a0.
[88] G. Christou, D. Gatteschi, D.N. Hendrickson, R. Sessoli, Single-molecule magnets, MRS Bull. 25 (2000) 66–71, https://doi.org/10.1557/mrs2000.226.
[89] O. Kahn, Molecular Magnetism, VCH, New York, 1993.
[90] B.O. Roos, R. Lindh, P.Å. Malmqvist, V. Veryazov, P.O. Widmark, Main group atoms and dimers studied with a new relativistic ANO basis set, J. Phys. Chem. A 108 (2004) 2851–2858, https://doi.org/10.1021/jp031064+.
[91] B.O. Roos, R. Lindh, P.Å. Malmqvist, V. Veryazov, P.O. Widmark, New relativistic ANO basis sets for transition metal atoms, J. Phys. Chem. A 109 (2005) 6575–6579, https://doi.org/10.1021/jp0581126.
[92] P.Å. Malmqvist, B.O. Roos, B. Schimmelpfennig, The restricted active space (RAS) state interaction approach with spin-orbit coupling, Chem. Phys. Lett. 357 (2002) 230–240, https://doi.org/10.1016/S0009-2614(02)00498-0.
[93] B.A. Heß, C.M. Marian, U. Wahlgren, O. Gropen, A mean-field spin-orbit method applicable to correlated wavefunctions, Chem. Phys. Lett. 251 (1996) 365–371, https://doi.org/10.1016/0009-2614(96)00119-4.
[94] T. Helgaker, P. Jørgensen, J. Olsen, Molecular Electronic-Structure Theory, Wiley, Chichester, 2000. http://eu.wiley.com/WileyCDA/WileyTitle/productCd-0471967556.html.

[95] B.O. Roos, R. Lindh, P. Malmqvist, V. Veryazov, P.O. Widmark, Multiconfigurational Quantum Chemistry, John Wiley & Sons, Inc., Hoboken, NJ, 2016, https://doi.org/10.1002/9781119126171.
[96] R. McWeeny, Methods of Molecular Quantum Mechanics, second ed., Academic Press, London, 1992.
[97] P.Å. Malmqvist, A. Rendell, B.O. Roos, The restricted active space self-consistent-field method, implemented with a split graph unitary group approach, J. Phys. Chem. 94 (1990) 5477–5482, https://doi.org/10.1021/j100377a011.
[98] D. Ma, G. Li Manni, L. Gagliardi, The generalized active space concept in multiconfigurational self-consistent field methods, J. Chem. Phys. 135 (2011), https://doi.org/10.1063/1.3611401.
[99] T. Fleig, J. Olsen, C.M. Marian, The generalized active space concept for the relativistic treatment of electron correlation. I. Kramers-restricted two-component configuration interaction, J. Chem. Phys. 114 (2001) 4775–4790, https://doi.org/10.1063/1.1349076.
[100] T. Fleig, J. Olsen, L. Visscher, The generalized active space concept for the relativistic treatment of electron correlation. II. Large-scale configuration interaction implementation based on relativistic 2- and 4-spinors and its application, J. Chem. Phys. 119 (2003) 2963–2971, https://doi.org/10.1063/1.1590636.
[101] F. Aquilante, J. Autschbach, R.K. Carlson, L.F. Chibotaru, M.G. Delcey, L. De Vico, I. Fdez Galván, N. Ferré, L.M. Frutos, L. Gagliardi, M. Garavelli, A. Giussani, C. E. Hoyer, G. Li Manni, H. Lischka, D. Ma, P.Å. Malmqvist, T. Müller, A. Nenov, M. Olivucci, T.B. Pedersen, D. Peng, F. Plasser, B. Pritchard, M. Reiher, I. Rivalta, I. Schapiro, J. Segarra-Martí, M. Stenrup, D.G. Truhlar, L. Ungur, A. Valentini, S. Vancoillie, V. Veryazov, V.P. Vysotskiy, O. Weingart, F. Zapata, R. Lindh, Molcas 8: new capabilities for multiconfigurational quantum chemical calculations across the periodic table, J. Comput. Chem. 37 (2016) 506–541, https://doi.org/10.1002/jcc.24221.
[102] G.L. Manni, S.D. Smart, A. Alavi, Combining the complete active space self-consistent field method and the full configuration interaction quantum Monte Carlo within a super-CI framework, with application to challenging metal-porphyrins, J. Chem. Theory Comput. 12 (2016) 1245–1258, https://doi.org/10.1021/acs.jctc.5b01190.
[103] N. Nakatani, S. Guo, Density matrix renormalization group (DMRG) method as a common tool for large active-space CASSCF/CASPT2 calculations, J. Chem. Phys. 146 (2017), https://doi.org/10.1063/1.4976644.
[104] F. Liu, Y. Kurashige, T. Yanai, K. Morokuma, Multireference ab initio density matrix renormalization group (DMRG)-CASSCF and DMRG-CASPT2 study on the photochromic ring opening of spiropyran, J. Chem. Theory Comput. 9 (2013) 4462–4469, https://doi.org/10.1021/ct400707k.
[105] Y. Kurashige, T. Yanai, High-performance ab initio density matrix renormalization group method: applicability to large-scale multireference problems for metal compounds, J. Chem. Phys. 130 (2009), https://doi.org/10.1063/1.3152576.
[106] K.H. Marti, M. Reiher, The density matrix renormalization group algorithm in quantum chemistry, Z. Phys. Chem. 224 (2010) 583–599, https://doi.org/10.1524/zpch.2010.6125.
[107] J. Finley, P.-Å. Malmqvist, B.O. Roos, L. Serrano-Andrés, The multi-state CASPT2 method, Chem. Phys. Lett. 288 (1998) 299–306, https://doi.org/10.1016/S0009-2614(98)00252-8.
[108] K. Pierloot, The CASPT2 method in inorganic electronic spectroscopy: from ionic transition metal to covalent actinide complexes, Mol. Phys. 101 (2003) 2083–2094, https://doi.org/10.1080/0026897031000109356.

[109] D. Ma, G. Li Manni, J. Olsen, L. Gagliardi, Second-order perturbation theory for generalized active space self-consistent-field wave functions, J. Chem. Theory Comput. 12 (2016) 3208–3213, https://doi.org/10.1021/acs.jctc.6b00382.
[110] S. Vancoillie, H. Zhao, V.T. Tran, M.F.A. Hendrickx, K. Pierloot, Multiconfigurational second-order perturbation theory restricted active space (RASPT2) studies on mononuclear first-row transition-metal systems, J. Chem. Theory Comput. 7 (2011) 3961–3977, https://doi.org/10.1021/ct200597h.
[111] V. Sauri, L. Serrano-Andrés, A.R.M. Shahi, L. Gagliardi, S. Vancoillie, K. Pierloot, Multiconfigurational second-order perturbation theory restricted active space (RASPT2) method for electronic excited states: a benchmark study, J. Chem. Theory Comput. 7 (2011) 153–168, https://doi.org/10.1021/ct100478d.
[112] K. Andersson, P.Å. Malmqvist, B.O. Roos, A.J. Sadlej, K. Wolinski, Second-order perturbation theory with a CASSCF reference function, J. Phys. Chem. 94 (1990) 5483–5488, https://doi.org/10.1021/j100377a012.
[113] K. Andersson, P.Å. Malmqvist, B.O. Roos, Second-order perturbation theory with a complete active space self-consistent field reference function, J. Chem. Phys. 96 (1992) 1218–1226, https://doi.org/10.1063/1.462209.
[114] C. Angeli, M. Pastore, R. Cimiraglia, New perspectives in multireference perturbation theory: the n-electron valence state approach, Theor. Chem. Acc. 117 (2007) 743–754, https://doi.org/10.1007/s00214-006-0207-0.
[115] Y. Guo, K. Sivalingam, E.F. Valeev, F. Neese, Explicitly correlated N-electron valence state perturbation theory (NEVPT2-F12), J. Chem. Phys. 147 (2017), https://doi.org/10.1063/1.4996560 064110.
[116] T. Shiozaki, W. Gyroffy, P. Celani, H.J. Werner, Communication: extended multi-state complete active space second-order perturbation theory: energy and nuclear gradients, J. Chem. Phys. 135 (2011), https://doi.org/10.1063/1.3633329.
[117] A.A. Granovsky, Extended multi-configuration quasi-degenerate perturbation theory: the new approach to multi-state multi-reference perturbation theory, J. Chem. Phys. 134 (2011) 214113, https://doi.org/10.1063/1.3596699.
[118] P.J. Knowles, H.J. Werner, Internally contracted multiconfiguration-reference configuration interaction calculations for excited states, Theor. Chim. Acta 84 (1992) 95–103, https://doi.org/10.1007/BF01117405.
[119] Y. Wang, H. Han, Y. Lei, B. Suo, H. Zhu, Q. Song, Z. Wen, New schemes for internally contracted multi-reference configuration interaction, J. Chem. Phys. 141 (2014) 164114, https://doi.org/10.1063/1.4898156.
[120] P.Å. Malmqvist, B.O. Roos, The CASSCF state interaction method, Chem. Phys. Lett. 155 (1989) 189–194, https://doi.org/10.1016/0009-2614(89)85347-3.
[121] B.O. Roos, P.-Å. Malmqvist, Relativistic quantum chemistry: the multiconfigurational approach, Phys. Chem. Chem. Phys. 6 (2004) 2919, https://doi.org/10.1039/b401472n.
[122] D. Gatteschi, A.L. Barra, A. Caneschi, A. Cornia, R. Sessoli, L. Sorace, EPR of molecular nanomagnets, Coord. Chem. Rev. 250 (2006) 1514–1529, https://doi.org/10.1016/j.ccr.2006.02.006.
[123] N. Iwahara, V. Vieru, L. Ungur, L.F. Chibotaru, Zeeman interaction and Jahn-Teller effect in the Γ_8 multiplet, Phys. Rev. B 96 (2017), https://doi.org/10.1103/PhysRevB.96.064416 064416.
[124] L.F. Chibotaru, Ab initio methodology for pseudospin hamiltonians of anisotropic magnetic complexes, in: Advances in Chemical Physics, John Wiley & Sons, Inc., 2013, pp. 397–519, https://doi.org/10.1002/9781118571767.ch6.

[125] H.J. Werner, P.J. Knowles, G. Knizia, F.R. Manby, M. Schütz, Molpro: a general-purpose quantum chemistry program package, Wiley Interdiscip. Rev. Comput. Mol. Sci. 2 (2012) 242–253, https://doi.org/10.1002/wcms.82.
[126] L.F. Chibotaru, L. Ungur, A. Soncini, The origin of nonmagnetic kramers doublets in the ground state of dysprosium triangles: evidence for a toroidal magnetic moment, Angew. Chem. Int. Ed. 47 (2008), https://doi.org/10.1002/anie.200800283.
[127] L. Ungur, Ab Initio Methodology for the Investigation of Magnetism in Strongly Anisotropic Complexes (Ph.D. thesis), Katholieke Universiteit Leuven, Belgium, 2010.
[128] L. Ungur, L.F. Chibotaru, Magnetic anisotropy in the excited states of low symmetry lanthanide complexes, Phys. Chem. Chem. Phys. 13 (2011) 20086, https://doi.org/10.1039/c1cp22689d.
[129] L. Ungur, M. Thewissen, J.-P. Costes, W. Wernsdorfer, L.F. Chibotaru, Interplay of strongly anisotropic metal ions in magnetic blocking of complexes, Inorg. Chem. 52 (2013) 6328–6337, https://doi.org/10.1021/ic302568x.
[130] Y.-C. Chen, J.-L. Liu, L. Ungur, J. Liu, Q.-W. Li, L.-F. Wang, Z.-P. Ni, L.F. Chibotaru, X.-M. Chen, M.-L. Tong, Symmetry-supported magnetic blocking at 20 K in pentagonal bipyramidal Dy(III) single-ion magnets, J. Am. Chem. Soc. 138 (2016), https://doi.org/10.1021/jacs.5b13584.
[131] J.-L. Liu, Y.-C. Chen, Y.-Z. Zheng, W.-Q. Lin, L. Ungur, W. Wernsdorfer, L.F. Chibotaru, M.-L. Tong, Switching the anisotropy barrier of a single-ion magnet by symmetry change from quasi-D_{5h} to quasi-O_h, Chem. Sci. 4 (2013), https://doi.org/10.1039/c3sc50843a.
[132] L. Ungur, J.J. Leroy, I. Korobkov, M. Murugesu, L.F. Chibotaru, Fine-tuning the local symmetry to attain record blocking temperature and magnetic remanence in a single-ion magnet, Angew. Chem. Int. Ed. 53 (2014) 4413–4417, https://doi.org/10.1002/anie.201310451.
[133] J.H. Van Vleck, The Theory of Electric and Magnetic Susceptibilities, Oxford Univ. Press, 1932. 384 pp. http://www.getcited.org/pub/101216313. Accessed 22 December 2017.
[134] H. Samata, N. Wada, T.C. Ozawa, Van Vleck paramagnetism of europium oxyhydroxide, J. Rare Earths 33 (2015) 177–181, https://doi.org/10.1016/S1002-0721(14)60399-9.
[135] D. Gatteschi, R. Sessoli, L. Sorace, Magnetic bistability in lanthanide-based molecular systems: the role of anisotropy and exchange interactions, Handb. Phys. Chem. Rare Earths (2016) 91–139, https://doi.org/10.1016/bs.hpcre.2016.09.003.
[136] P.-H. Lin, T.J. Burchell, L. Ungur, L.F. Chibotaru, W. Wernsdorfer, M. Murugesu, A polinuclear lanthanide single-molecule magnet with a record anisotropic barrier, Angew. Chem. Int. Ed. 48 (2009). https://doi.org/10.1002/anie.200903199.
[137] C.A.P. Goodwin, F. Ortu, D. Reta, N.F. Chilton, D.P. Mills, Molecular magnetic hysteresis at 60 Kelvin in dysprosocenium, Nature 548 (2017) 439–442, https://doi.org/10.1038/nature23447.
[138] Y.S. Ding, N.F. Chilton, R.E.P. Winpenny, Y.Z. Zheng, On approaching the limit of molecular magnetic anisotropy: a near-perfect pentagonal bipyramidal dysprosium(III) single-molecule magnet, Angew. Chem. Int. Ed. 55 (2016), https://doi.org/10.1002/anie.201609685.
[139] L. Ungur, L.F. Chibotaru, Strategies toward high-temperature lanthanide-based single-molecule magnets, Inorg. Chem. 55 (2016) 10043–10056, https://doi.org/10.1021/acs.inorgchem.6b01353.
[140] L.F. Chibotaru, Theoretical Understanding of Anisotropy in Molecular Nanomagnets, Springer, Berlin, Heidelberg, 2014, pp. 185–229, https://doi.org/10.1007/430_2014_171.

[141] J. Villain, F. Hartman-Boutron, R. Sessoli, A. Rettori, Magnetic relaxation in big magnetic molecules, Europhys. Lett. 27 (1994) 159–164, https://doi.org/10.1209/0295-5075/27/2/014.
[142] M.A. Novak, W.S.D. Folly, J.P. Sinnecker, S. Soriano, Relaxation in magnetic nanostructures, J. Magn. Magn. Mater. (2005) 133–140, https://doi.org/10.1016/j.jmmm.2005.03.026.
[143] M. Leuenberger, D. Loss, Spin tunneling and phonon-assisted relaxation in Mn_{12}-acetate, Phys. Rev. B 61 (2000) 1286–1302, https://doi.org/10.1103/PhysRevB.61.1286.
[144] F. Hartmann-boutron, P. Politi, J. Villain, Tunneling and magnetic relaxation in mesoscopic molecules, Int. J. Mod. Phys. B 10 (1996) 2577–2637, https://doi.org/10.1142/S0217979296001148.
[145] F. Luis, M.J. Martínez-Pérez, O. Montero, E. Coronado, S. Cardona-Serra, C. Martí-Gastaldo, J.M. Clemente-Juan, J. Sesé, D. Drung, T. Schurig, Spin-lattice relaxation via quantum tunneling in an Er^{3+} -polyoxometalate molecular magnet, Phys. Rev. B: Condens. Matter Mater. Phys. 82 (2010) 3–6, https://doi.org/10.1103/PhysRevB.82.060403.
[146] V. Dohm, P. Fulde, Magnetoelastic interaction in rare earth systems, Z. Phys. B: Condens. Matter 21 (1975) 369–379, https://doi.org/10.1007/PL00020764.
[147] D.A. Garanin, E.M. Chudnovsky, Thermally activated resonant magnetization tunneling in molecular magnets: Mn_{12}Ac and others, Phys. Rev. B 56 (1997) 11102–11118, https://doi.org/10.1103/PhysRevB.56.11102.
[148] E.M. Chudnovsky, J. Tejada, Macroscopic Quantum Tunneling of the Magnetic Moment, Cambridge University Press, 1998, https://doi.org/10.1017/CBO9780511524219.
[149] R.J. Blagg, L. Ungur, F. Tuna, J. Speak, P. Comar, D. Collison, W. Wernsdorfer, E.J.L. McInnes, L.F. Chibotaru, R.E.P. Winpenny, Magnetic relaxation pathways in lanthanide single-molecule magnets, Nat. Chem. 5 (2013) 673–678, https://doi.org/10.1038/nchem.1707.
[150] N.F. Chilton, C.A.P. Goodwin, D.P. Mills, R.E.P. Winpenny, The first near-linear bis(amide) f-block complex: a blueprint for a high temperature single molecule magnet, Chem. Commun. 51 (2015) 101–103, https://doi.org/10.1039/C4CC08312A.
[151] Y.-N. Guo, L. Ungur, G.E. Granroth, A.K. Powell, C. Wu, S.E. Nagler, J. Tang, L.F. Chibotaru, D. Cui, An NCN-pincer ligand dysprosium single-ion magnet showing magnetic relaxation via the second excited state, Sci. Rep. 4 (2014) 5471, https://doi.org/10.1038/srep05471.
[152] J. Liu, Y.-C. Chen, J.-L. Liu, V. Vieru, L. Ungur, J.-H. Jia, L.F. Chibotaru, Y. Lan, W. Wernsdorfer, S. Gao, X.-M. Chen, M.-L. Tong, A stable pentagonal bipyramidal Dy(III) single-ion magnet with a record magnetization reversal barrier over 1000 K, J. Am. Chem. Soc. 138 (16) (2016) 5441–5450, https://doi.org/10.1021/jacs.6b02638.
[153] F.S. Guo, B.M. Day, Y.C. Chen, M.L. Tong, A. Mansikkamäki, R.A. Layfield, A dysprosium metallocene single-molecule magnet functioning at the axial limit, Angew. Chem. Int. Ed. 56 (38) (2017) 11445–11449, https://doi.org/10.1002/anie.201705426.
[154] S.K. Singh, T. Gupta, M. Shanmugam, G. Rajaraman, Unprecedented magnetic relaxation via the fourth excited state in low-coordinate lanthanide single-ion magnets: a theoretical perspective, Chem. Commun. 50 (2014) 15513–15516, https://doi.org/10.1039/C4CC05522E.
[155] J. Sievers, Asphericity of 4f-shells in their Hund's rule ground states, Z. Phys. B: Condens. Matter 45 (1982) 289–296, https://doi.org/10.1007/BF01321865.

[156] J.D. Rinehart, J.R. Long, Exploiting single-ion anisotropy in the design of f-element single-molecule magnets, Chem. Sci. 2 (2011) 2078, https://doi.org/10.1039/c1sc00513h.
[157] M.A.H. Brian, N. Figgis, Ligand Field Theory and Its Applications, Wiley-VCH, New York, 2000.
[158] J.J. Le Roy, M. Jeletic, S.I. Gorelsky, I. Korobkov, L. Ungur, L.F. Chibotaru, M. Murugesu, An organometallic building block approach to produce a multidecker 4f single-molecule magnet, J. Am. Chem. Soc. 135 (2013), https://doi.org/10.1021/ja310642h.
[159] K.R. Meihaus, J.R. Long, Magnetic blocking at 10 K and a dipolar-mediated avalanche in salts of the bis(η8-cyclooctatetraenide) complex [Er(COT)$_2$], J. Am. Chem. Soc. 135 (2013), https://doi.org/10.1021/ja4094814.
[160] N.F. Chilton, Design criteria for high-temperature single-molecule magnets, Inorg. Chem. 54 (2015) 2097–2099, https://doi.org/10.1021/acs.inorgchem.5b00089.
[161] J.-L. Liu, J.-Y. Wu, Y.-C. Chen, V. Mereacre, A.K. Powell, L. Ungur, L.F. Chibotaru, X.-M. Chen, M.-L. Tong, A heterometallic Fe^{II}-Dy^{III} single-molecule magnet with a record anisotropy barrier, Angew. Chem. Int. Ed. 53 (2014)https://doi.org/10.1002/anie.201407799.
[162] S.K. Gupta, T. Rajeshkumar, G. Rajaraman, R. Murugavel, An air-stable Dy(III) single-ion magnet with high anisotropy barrier and blocking temperature, Chem. Sci. 7 (2016), https://doi.org/10.1039/C6SC00279J.
[163] K.L.M. Harriman, J.L. Brosmer, L. Ungur, P.L. Diaconescu, M. Murugesu, Pursuit of record breaking energy barriers: a study of magnetic axiality in diamide ligated Dy^{III} single-molecule magnets, J. Am. Chem. Soc. 139 (2017) 1420–1423, https://doi.org/10.1021/jacs.6b12374.
[164] K.S. Pedersen, L. Ungur, M. Sigrist, A. Sundt, M. Schau-Magnussen, V. Vieru, H. Mutka, S. Rols, H. Weihe, O. Waldmann, L.F. Chibotaru, J. Bendix, J. Dreiser, Modifying the properties of 4f single-ion magnets by peripheral ligand functionalisation, Chem. Sci. 5 (2014) 1650–1660, https://doi.org/10.1039/C3SC53044B.
[165] B.M. Flanagan, P.V. Bernhardt, E.R. Krausz, S.R. Lüthi, M.J. Riley, A ligand-field analysis of the trensal (H3trensal = 2,2′,2″-tris(salicylideneimino)triethylamine) ligand. An application of the angular overlap model to lanthanides, Inorg. Chem. 41 (2002) 5024–5033, https://doi.org/10.1021/ic011276q.
[166] B.M. Flanagan, P.V. Bernhardt, E.R. Krausz, S.R. Lüthi, M.J. Riley, Ligand-field analysis of an Er(III) complex with a heptadentate tripodal N_4O_3 ligand, Inorg. Chem. 40 (2001) 5401–5407, https://doi.org/10.1021/ic0103244.
[167] B.O. Roos, R. Lindh, P.-Å. Malmqvist, V. Veryazov, P.-O. Widmark, A.C. Borin, New relativistic atomic natural orbital basis sets for lanthanide atoms with applications to the Ce diatom and LuF_3, J. Phys. Chem. A 112 (2008) 11431–11435, https://doi.org/10.1021/jp803213j.
[168] G. Ghigo, B.O. Roos, P.Å. Malmqvist, A modified definition of the zeroth-order Hamiltonian in multiconfigurational perturbation theory (CASPT2), Chem. Phys. Lett. 396 (2004) 142–149, https://doi.org/10.1016/j.cplett.2004.08.032.
[169] P.Å. Malmqvist, K. Pierloot, A.R.M. Shahi, C.J. Cramer, L. Gagliardi, The restricted active space followed by second-order perturbation theory method: theory and application to the study of CuO_2 and Cu_2O_2 systems, J. Chem. Phys. 128 (2008) 204109, https://doi.org/10.1063/1.2920188.
[170] S. Vancoillie, M.G. Delcey, R. Lindh, V. Vysotskiy, P.-Å. Malmqvist, V. Veryazov, Parallelization of a multiconfigurational perturbation theory, J. Comput. Chem. 34 (2013) 1937–1948, https://doi.org/10.1002/jcc.23342.

[171] D. Aravena, M. Atanasov, F. Neese, Periodic trends in lanthanide compounds through the eyes of multireference ab initio theory, Inorg. Chem. 55 (2016) 4457–4469, https://doi.org/10.1021/acs.inorgchem.6b00244.
[172] S. Tsukamoto, H. Mori, H. Tatewaki, E. Miyoshi, CASSCF and CASPT2 calculations for lanthanide trihalides LnX3 using model core potentials, Chem. Phys. Lett. 474 (2009) 28–32, https://doi.org/10.1016/J.CPLETT.2009.04.018.
[173] E. Ruiz, J. Cano, S. Alvarez, P. Alemany, Broken symmetry approach to calculation of exchange coupling constants for homobinuclear and heterobinuclear transition metal complexes, J. Comput. Chem. 20 (1999) 1391–1400, https://doi.org/10.1002/(SICI)1096-987X(199910)20:13<1391::AID-JCC6>3.0.CO;2-J.
[174] M.E. Lines, Orbital angular momentum in the theory of paramagnetic clusters, J. Chem. Phys. 55 (1971) 2977–2984, https://doi.org/10.1063/1.1676524.
[175] M. Gysler, F. El Hallak, L. Ungur, R. Marx, M. Hakl, P. Neugebauer, Y. Rechkemmer, Y. Lan, I. Sheikin, M. Orlita, C.E. Anson, A.K. Powell, R. Sessoli, L.F. Chibotaru, J. Van Slageren, Multitechnique investigation of Dy_3-implications for coupled lanthanide clusters, Chem. Sci. 7 (2016), https://doi.org/10.1039/c6sc00318d.
[176] J. Luzon, K. Bernot, I.J. Hewitt, C.E. Anson, A.K. Powell, R. Sessoli, Spin chirality in a molecular dysprosium triangle: the archetype of the noncollinear ising model, Phys. Rev. Lett. 100 (2008) 247205, https://doi.org/10.1103/PhysRevLett.100.247205.
[177] L. Ungur, W. Van Den Heuvel, L.F. Chibotaru, Ab initio investigation of the non-collinear magnetic structure and the lowest magnetic excitations in dysprosium triangles, New J. Chem. 33 (2009), https://doi.org/10.1039/b903126j.
[178] L. Ungur, S.-Y. Lin, J. Tang, L.F. Chibotaru, Single-molecule toroics in Ising-type lanthanide molecular clusters, Chem. Soc. Rev. 43 (2014) 6894–6905, https://doi.org/10.1039/C4CS00095A.
[179] S.Y. Lin, W. Wernsdorfer, L. Ungur, A.K. Powell, Y.N. Guo, J. Tang, L. Zhao, L.F. Chibotaru, H.J. Zhang, Coupling Dy3 triangles to maximize the toroidal moment, Angew. Chem. Int. Ed. (2012) https://doi.org/10.1002/anie.201206602.
[180] L. Ungur, S.K. Langley, T.N. Hooper, B. Moubaraki, E.K. Brechin, K.S. Murray, L.F. Chibotaru, Net toroidal magnetic moment in the ground state of a $\{Dy_6\}$-triethanolamine ring, J. Am. Chem. Soc. 134 (45) (2012) 18554–18557, https://doi.org/10.1021/ja309211d.
[181] K.R. Vignesh, A. Soncini, S.K. Langley, W. Wernsdorfer, K.S. Murray, G. Rajaraman, Ferrotoroidic ground state in a heterometallic $\{Cr^{III}Dy^{III}6\}$ complex displaying slow magnetic relaxation, Nat. Commun. 8 (2017) 1023, https://doi.org/10.1038/s41467-017-01102-5.
[182] A.I. Popov, D.I. Plokhov, A.K. Zvezdin, Anapole moment and spin-electric interactions in rare-earth nanoclusters, Europhys. Lett. 87 (2009) 67004, https://doi.org/10.1209/0295-5075/87/67004.
[183] M. Trif, F. Troiani, D. Stepanenko, D. Loss, Spin electric effects in molecular antiferromagnets, Phys. Rev. B 82 (2010)45429, https://doi.org/10.1103/PhysRevB.82.045429.
[184] J.A. Mydosh, Reports on progress in physics, Rep. Prog. Phys. 78 (2015) 52501, https://doi.org/10.1088/0034-4885/78/5/052501.
[185] C. Weingart, N. Spaldin, E. Bousquet, Noncollinear magnetism and single-ion anisotropy in multiferroic perovskites, Phys. Rev. B: Condens. Matter Mater. Phys. 86 (2012) 94413, https://doi.org/10.1103/PhysRevB.86.094413.
[186] E. Bousquet, A. Cano, Non-collinear magnetism in multiferroic perovskites, J. Phys. Condens. Matter 28 (2016) 123001, https://doi.org/10.1088/0953-8984/28/12/123001.

[187] U. Valiev, A. Zvezdin, G. Krinchik, Faraday effect of rare-earth iron garnets in strong magnetic fields, Zh. Eksp. Teor. Fiz. 327 (1983) 181–189. http://www.jetp.ac.ru/cgi-bin/dn/e_058_01_0181.pdf. Accessed 22 December 2017.
[188] K.C. Mondal, A. Sundt, Y. Lan, G.E. Kostakis, O. Waldmann, L. Ungur, L.F. Chibotaru, C.E. Anson, A.K. Powell, Coexistence of distinct single-ion and exchange-based mechanisms for blocking of magnetization in a $Co^{II}2Dy^{III}2$ single-molecule magnet, Angew. Chem. Int. Ed. 51 (2012), https://doi.org/10.1002/anie.201201478.
[189] G. Novitchi, G. Pilet, L. Ungur, V.V. Moshchalkov, W. Wernsdorfer, L.F. Chibotaru, D. Luneau, A.K. Powell, Heterometallic Cu^{II}/Dy^{III} 1D chiral polymers: chirogenesis and exchange coupling of toroidal moments in trinuclear Dy_3 single molecule magnets, Chem. Sci. 3 (2012), https://doi.org/10.1039/c2sc00728b.
[190] S.K. Langley, L. Ungur, N.F. Chilton, B. Moubaraki, L.F. Chibotaru, K.S. Murray, Single-molecule magnetism in a family of $\{Co^{III}2Dy^{III}2\}$ butterfly complexes: effects of ligand replacement on the dynamics of magnetic relaxation, Inorg. Chem. 53 (2014), https://doi.org/10.1021/ic4029645.
[191] L.F. Chibotaru, L. Ungur, C. Aronica, H. Elmoll, G. Pilet, D. Luneau, Structure, magnetism, and theoretical study of a mixed-valence $Co^{II}3Co^{III}4$ heptanuclear wheel: lack of SMM behavior despite negative magnetic anisotropy, J. Am. Chem. Soc. 130 (2008) 12445–12455, https://doi.org/10.1021/ja8029416.
[192] A. Bhunia, M.T. Gamer, L. Ungur, L.F. Chibotaru, A.K. Powell, Y. Lan, P.W. Roesky, F. Menges, C. Riehn, G. Niedner-Schatteburg, From a Dy(III) single molecule magnet (SMM) to a ferromagnetic [Mn(II)Dy(III)Mn(II)] trinuclear complex, Inorg. Chem. 51 (2012) 9589–9597, https://doi.org/10.1021/ic300065x.
[193] A. Lunghi, F. Totti, S. Sanvito, R. Sessoli, Intra-molecular origin of the spin-phonon coupling in slow-relaxing molecular magnets, Chem. Sci. (2017), https://doi.org/10.1039/C7SC02832F.
[194] A. Lunghi, F. Totti, R. Sessoli, S. Sanvito, The role of anharmonic phonons in under-barrier spin relaxation of single molecule magnets, Nat. Commun. 8 (2017), https://doi.org/10.1038/ncomms14620.
[195] S. Gómez-Coca, A. Urtizberea, E. Cremades, P.J. Alonso, A. Camón, E. Ruiz, F. Luis, Origin of slow magnetic relaxation in Kramers ions with non-uniaxial anisotropy, Nat. Commun. 5 (2014)4300, https://doi.org/10.1038/ncomms5300.
[196] F. Aquilante, P.Å. Malmqvist, T.B. Pedersen, A. Ghosh, B.O. Roos, Cholesky decomposition-based multiconfiguration second-order perturbation theory (CD-CASPT2): application to the spin-state energetics of Co^{III}(diiminato)(NPh), J. Chem. Theory Comput. 4 (2008) 694–702, https://doi.org/10.1021/ct700263h.
[197] H. Koch, A. Sánchez de Merás, T.B. Pedersen, Reduced scaling in electronic structure calculations using Cholesky decompositions, J. Chem. Phys. 118 (2003) 9481–9484, https://doi.org/10.1063/1.1578621.
[198] R. Polly, H.-J. Werner, F.R. Manby, P.J. Knowles, Fast Hartree–Fock theory using local density fitting approximations, Mol. Phys. 102 (2004) 2311–2321, https://doi.org/10.1080/00268970420002748O1.
[199] D.B. Krisiloff, C.M. Krauter, F.J. Ricci, E.A. Carter, Density fitting and cholesky decomposition of the two-electron integrals in local multireference configuration interaction theory, J. Chem. Theory Comput. 11 (2015) 5242–5251, https://doi.org/10.1021/acs.jctc.5b00762.
[200] W. Van den Heuvel, S. Calvello, A. Soncini, Configuration-averaged 4f orbitals in ab initio calculations of low-lying crystal field levels in lanthanide(III) complexes, Phys. Chem. Chem. Phys. 18 (2016) 15807–15814, https://doi.org/10.1039/C6CP02325H.

[201] P.P. Hallmen, C. Köppl, G. Rauhut, H. Stoll, J. van Slageren, Fast and reliable ab initio calculation of crystal field splittings in lanthanide complexes, J. Chem. Phys. 147 (2017) 164101, https://doi.org/10.1063/1.4998815.
[202] S. Calvello, M. Piccardo, S.V. Rao, A. Soncini, CERES: an ab initio code dedicated to the calculation of the electronic structure and magnetic properties of lanthanide complexes, J. Comput. Chem. 39 (6) (2017) 328–337, https://doi.org/10.1002/jcc.25113.

Biography

Liviu Ungur graduated in Chemistry at the State University of Moldova (Chisinau) in 2005, and received his Ph.D. from the University of Leuven, Belgium, in 2010, under the supervision of Prof. Liviu F. Chibotaru. In 2011–17 he was a fellow of the Flemish Science Foundation. In 2015–16 he worked at University of Lund with Per-Ake Malmqvist and Valera Veryazov. He received the Best PhD Thesis in Molecular Magnetism from the European Institute of Molecular Magnetism in June 2014. He is presently working in the Theory of Nanomaterials group at KU Leuven with Prof. Liviu F. Chibotaru. His research is oriented toward the development and application of novel approaches for the theoretical description of magnetism and magnetic interactions in mono- and polynuclear compounds containing strongly anisotropic metal sites, as well as investigation of electronic structures, optic and magnetic properties of magnetic molecules deposited on various surfaces. Since June 2018 he is appointed at the Department of Chemistry at the National University of Singapore.